

# Electromyogram (EMG) Removal by Adding Sources of EMG (ERASE) - A novel ICA-based algorithm for removing myoelectric artifacts from EEG - Part 1

Yongcheng Li<sup>1</sup>, Po T. Wang<sup>2</sup>, Mukta P. Vaidya<sup>3,4,5</sup>, Charles Y. Liu<sup>6,7,8</sup>, Marc W. Slutzky<sup>3,4,5</sup> and An H. Do<sup>1</sup>

<sup>1</sup> Department of Neurology, University of California, Irvine, CA 92697 USA

<sup>2</sup> Department of Biomedical Engineering, University of California, Irvine, CA 92697, USA

<sup>3</sup> Department of Neurology, Northwestern University, Chicago, Illinois, USA

<sup>4</sup> Department of Physiology, Northwestern University, Chicago, Illinois, USA

<sup>5</sup> Department of Physical Medicine and Rehabilitation, Northwestern University, Chicago, Illinois, USA

<sup>6</sup> Department of Neurosurgery, University of Southern California, CA, USA

<sup>7</sup> Rancho Los Amigos National Rehabilitation Center, CA, USA

<sup>8</sup> Neurorestoration Center, University of Southern California, CA, USA

E-mail: and@uci.edu; yongchel@uci.edu

**Abstract.** Electroencephalographic (EEG) recordings are often contaminated by electromyographic (EMG) artifacts, especially when recording during movement. Existing methods to remove EMG artifacts include independent component analysis (ICA), and other high-order statistical methods. However, these methods can not effectively remove most of EMG artifacts. Here, we proposed a modified ICA model for EMG artifacts removal in the EEG, which is called EMG Removal by Adding Sources of EMG (ERASE). In this new approach, additional channels of real EMG from neck and head muscles (reference artifacts) were added as inputs to ICA in order to “force” the most power from EMG artifacts into a few independent components (ICs). The ICs containing EMG artifacts (the “artifact ICs”) were identified and rejected using an automated procedure. ERASE was validated first using both simulated and experimentally-recorded EEG and EMG. Simulation results showed ERASE removed EMG artifacts from EEG significantly more effectively than conventional ICA. Also, it had a low false positive rate and high sensitivity. Subsequently, EEG was collected from 8 healthy participants while they moved their hands to test the realistic efficacy of this approach. Results showed that ERASE successfully removed EMG artifacts (on average, about 75% of EMG artifacts were removed when using real EMGs as reference artifacts) while preserving the expected EEG features related to movement. We also tested the ERASE procedure using simulated EMGs as reference artifacts (about 63% of EMG artifacts removed). Compared to conventional ICA, ERASE removed on average 26% more EMG artifacts from EEG. These findings suggest that ERASE can achieve significant separation of EEG signal and EMG artifacts without a loss of the underlying EEG features. These results indicate that using additional real or simulated EMG sources can increase the effectiveness of ICA in removing EMG artifacts from

EEG. Combined with automated artifact IC rejection, ERASE also minimizes potential user bias. Future work will focus on improving ERASE so that it can also be used in real-time applications.

artifacts removal, ICA, electroencephalogram (EEG), muscle artifacts, neural network

## 1. Introduction

Electroencephalographic (EEG) signals are often contaminated by surface electromyographic (EMG) signals and can make it difficult to appropriately interpret EEG signals or use them in various neuroengineering applications. There are many approaches to remove EMG artifacts from EEG signals, which can be broadly classified in the following categories [1–4]: 1). filtering (e.g. adaptive filtering, Wiener filtering, and Bayes filtering [5–7]), 2). linear regression method [8–10], 3). blind source separation (BSS) methods which includes principal component analysis (PCA) [11, 12], independent component analysis (ICA) [13–16], canonical correlation analysis (CCA) [17–20], sparse component analysis (SCA) [21], singular spectrum analysis (SSA) [22], and etc. 4). source decomposition, including discrete wavelet transform (DWT) [17, 23–25], empirical mode decomposition (EMD) [26–28], stationary wavelet transform (SWT) [29, 30] and ensemble empirical mode decomposition (EEMD) [20, 31–33], 5). neural networks (NN) [34, 35] and adaptive neural fuzzy inference systems (ANFIS) [36, 37]. In the setting of a plethora of EMG artifacts removal algorithms, previous surveys [1, 3] suggest that BSS methods are the most commonly used and outperform other approaches at EMG artifacts removal from EEG. Among the BSS methods mentioned above, Urigen et al [3] states that 45% of work in their bibliography use ICA to remove the EMG artifact from EEG. CCA is another widely employed method for the removal of EMG artifacts from EEG in recent years [19, 38]. However, it does not outperform ICA at removing EMG artifacts from EEG [17, 39, 40] or at removing ocular and cardiac artifacts [41–46].

Despite the popularity of ICA for EMG artifact rejection in EEG, its use is still affected by several issues [1, 47, 48]. For example, nearly all EEG channels are typically contaminated by EMG, and there is a high spatiotemporal overlap between EMG artifacts and EEG signal [49]. Therefore, conventional ICA algorithms are usually unable to separate EMG artifacts from the EEG signal—that is, it is difficult to “force” all of the EMG artifacts into an isolated set of independent components. Hence, post-ICA-treated data may still include residual EMG [49, 50]. Also, since the EMGs could have multiple source locations and show a large overlap with the higher frequency components (>20 Hz) of EEG signals, it is difficult to assign a universal operational definition for EMG components [51, 52]. Hence, rejection of EMG artifact components is typically performed manually *when no prior knowledge about artifacts is available*. This leads to potential over- or under-rejection of components as users attempt to distinguish between neurogenic and myogenic components in common ICA. Further, rejecting components manually is cumbersome/time-consuming and can introduce subjectivity. Additionally, accurate extraction of source signals in the ICA model is another issue since the global optimum in these algorithms is typically affected by the contrast function. Some approaches, which are presented in further detail below, were developed to solve these issues.

Some studies demonstrated that prior knowledge about artifacts or source signals can improve the effectiveness of ICA at removing artifacts [3, 57]. Therefore, constrained

ICA (cICA) or ICA with reference (ICA-R) which incorporate prior knowledge about the artifact and/or source signals were developed [13]. This is performed by imposing temporal or spatial constraints on the source mixture model. In temporally constrained ICA, prior knowledge about artifacts can be introduced into the ICA model to identify the artifact IC/ICs by solving a constrained optimization problem [13, 41, 53–55]. Temporally constrained ICA can only be used for the removal of EOG and ECG, but is not highly effective for EMG artifacts [41, 54, 55]. EMG artifacts sources, which are more time-varying and non-stationarity, are too complicated to characterize for optimization constraints. Hence, no prior studies have adequately addressed the separation of spatiotemporal overlap between EMG and EEG by using temporally constrained ICA. Spatially constrained ICA incorporates prior knowledge or assumption of spatial topographies of some source projections acting as a spatial filter, and limit the degree to which some of the columns of the mixing matrix may deviate from the known projections [12, 56–58]. As mentioned above, EMG artifacts are time-varying and highly overlapped with EEG. Hence, known spatial topographies of EMG source projections derived from previous data recording or mathematically simulated model are usually inaccurate and difficult to achieve. Although some work on EMG artifact removal utilized spatially constrained ICA with EEG during seizures [56], the performance of spatially constrained ICA on these ictal EEG, where the ground truth of EMG artifacts is actually unknown, has not been fully and rigorously established. Hence, using spatially constrained ICA to remove the EMG artifacts from real EEG is still unsubstantiated. Additionally, running ICA iteratively is required for both types of constrained ICA to reject the artifacts, which is time-consuming and hard to achieve real-time application. Even so, when the prior knowledge about artifacts or source signal is available, some form of spatially constrained ICA is preferred as compared to using ICA alone [3, 57].

Another important issue associated with removing EMG artifacts from EEG via ICA is automated EMG artifact rejection. Generally, *when reference waveforms are available*, there is one method to achieve automated rejection based on ICA in previous studies [3]. Specifically, cICA compares spatial and temporal statistical characteristics of ICs to those from background EEG or artifacts. Subsequently, a combination of thresholds for those statistical characteristics is used in an automated algorithm to reject the artifacts [14, 16, 47, 59, 60]. This method has been demonstrated to reliably remove EOG and ECG artifacts, particularly since these signals drastically differ from EEG in spatial and temporal statistical characteristics [41, 42, 61]. However, using this method for EMG artifact removal is still inadequate due to the spatiotemporal overlap between EMG artifacts and EEG signals (i.e. EMG artifacts always introduce a large number of unique scalp maps, leaving few ICs available for capturing brain sources). Therefore, it is necessary to develop an automated technique that can more effectively and systematically remove EMG artifacts while not affecting any of the underlying signal features.

In order to improve the effectiveness and reliability of ICA in removing the EMG artifacts from EEG and establish an effective automated artifacts rejection procedure,

we introduce a novel method, termed as *EMG Removal by Adding Sources of EMG* (ERASE) and subject it to rigorous mathematical and experimental validation. ERASE combines the advantages of two types of cICA. It aims to improve upon ICA by adding either real or simulated EMG artifacts as extra “reference” channel signals into the EEG data. We mathematically demonstrated that if the reference EMG artifacts were not independent of the contaminant EMG artifacts in EEG, a larger proportion of the artifacts could be identified by several specific independent components (ICs) after running ICA. Also, we proposed criteria based on the mixing matrix to automatically identify and reject the artifacts components. Our results revealed that ERASE had higher effectiveness in removing the EMG artifacts compared to conventional ICA. In summary, this study developed an effective EMG rejection approach, which can provide more confidence for the utilization of EEG in applications such as physiological studies underlying motor behaviors.

## 2. Methods

### 2.1. Description of ERASE ICA model based on added EMG sources

*2.1.1. Model description* To facilitate more effective removal of EMG artifacts from the EEG data, we combined EMG artifacts (here, either simulated EMG or recorded EMG) with EEG datasets and applied a modified ICA model as follows:

$$\begin{pmatrix} \hat{X}_t \\ n_\tau^* \end{pmatrix} = A_{t+\tau} \times S_{t+\tau}$$

$$\begin{pmatrix} X_t + b_t \cdot N_t \\ n_\tau^* \end{pmatrix} = A_{t+\tau} \times \begin{pmatrix} s_t + m_t \\ m_\tau^* \end{pmatrix} \quad (1)$$

where  $t$  is the number of the EEG channels ( $t$  dimension), and  $\tau$  is the number of the reference EMG channels ( $\tau$  dimension),  $\hat{X}_t = X_t + b_t \cdot N_t$ , and  $X_t$  is the uncontaminated EEG data;  $N_t$  is the contaminant EMG artifacts, which usually is the real EMG artifacts inside of EEG;  $b_t$  is the linear coefficients;  $n_\tau^*$  is the reference EMG artifacts, which are extra channels containing EMG signals from muscles or simulation;  $A_{t+\tau}$  is the mixing matrix of dimension  $(t + \tau) \times (t + \tau)$ ,  $S_{t+\tau}$  is the independent component sources with  $t + \tau$  dimension, in which  $s_t$  is the sources representing the uncontaminated EEG,  $m_t$  are the sources representing the contaminant EMG artifacts,  $m_\tau^*$  are the reference EMG sources.

**Theorem:** Given that the reference EMG sources are independent, and  $n_\tau^*$  is only dependent with  $N_t$ , then  $m_t = 0$ .

**Proof:** We assume that  $m_t \neq 0$ . In this model,  $N_t = a1_t \times m_t + a2_\tau \times m_\tau^*$  and  $n_\tau^* = a3_t \times m_t + a4_\tau \times m_\tau^*$  ( $a1$ ,  $a2$ ,  $a3$  and  $a4$  are the corresponding submatrices of the mixing matrix). Since  $N_t$  is dependent with  $n_\tau^*$ , a relationship can be defined as follows:

$$\mathbf{Y} := (y(N_t(1)), y(N_t(2)), \dots, y(N_t(m)), y(n_\tau^*(1)), y(n_\tau^*(2)), \dots, y(n_\tau^*(n)))$$

$$(m \leq t, n \leq \tau) \quad (2)$$

where  $y(\cdot)$  is probability density function.

This expression of  $N_t$  and  $n_\tau^*$  can be combined as follows:

$$\begin{aligned} \mathbf{Y} := & (y(a_{1t} \times m_t(1) + a_{2\tau} \times m_\tau^*(1)), y(a_{1t} \times m_t(2) + a_{2\tau} \times m_\tau^*(2)) \\ & , \dots, y(a_{1t} \times m_t(m) + a_{2\tau} \times m_\tau^*(m)), \\ & y(a_{3t} \times m_t(1) + a_{4\tau} \times m_\tau^*(1)), y(a_{3t} \times m_t(2) + a_{4\tau} \times m_\tau^*(2)) \\ & , \dots, y(a_{3t} \times m_t(n) + a_{4\tau} \times m_\tau^*(n))) \quad (m \leq t, n \leq \tau) \end{aligned} \quad (3)$$

Given that:  $z(m_t, m_\tau^*) = y(a_t \times m_t + a_\tau \times m_\tau^*)$ . We get:

$$\mathbf{Z} := (z(m_t(1)), z(m_t(2)), \dots, z(m_t(m)), z(m_\tau^*(1)), z(m_\tau^*(2)), \dots, z(m_\tau^*(n))) \quad (m \leq t, n \leq \tau) \quad (4)$$

where  $z(\cdot)$  is another expression of  $y(\cdot)$ ,  $N_t(m)$  is the contaminant artifacts in the  $m^{th}$  channel,  $n_\tau^*(n)$  is the reference EMG artifacts in the  $n^{th}$  channel,  $m_t(i)$  is the  $i^{th}$  sources representing the contaminant EMG artifacts, and  $m_\tau^*(j)$  is the  $j^{th}$  reference EMG sources. From the equation (4), we know that  $m_t$  is dependent with  $m_\tau^*$ . This denotes that the reference EMG source are dependent with sources representing contaminant EMG artifacts. Since this violates the ICA principle of component independence,  $m_t$  must equal 0.

Two key assumptions are made in our model. One is the independence among the reference EMG sources and the other was the dependence between the contaminant EMG artifacts and the reference EMG artifacts. This means if the simulated EMG can meet these two assumptions, in situations where real EMG was not collected, or the situation does not allow for EMG recordings, simulated EMG can also act as the reference EMG artifacts.

*2.1.2. Rejection criteria* We define the  $(t+\tau) \times (t+\tau)$  mixing matrix  $A_{t+\tau}$  in equation (1) as below:

$$A_{t+\tau} = \begin{pmatrix} a_{1,1} & a_{1,2} & \cdots & a_{1,t+\tau} \\ a_{2,1} & a_{2,2} & \cdots & a_{2,t+\tau} \\ \vdots & \vdots & \ddots & \vdots \\ a_{t,1} & a_{t,2} & \cdots & a_{t,t+\tau} \\ a_{t+1,1} & a_{t+1,2} & \cdots & a_{t+1,t+\tau} \\ \vdots & \vdots & \ddots & \vdots \\ a_{t+\tau,1} & a_{t+\tau,2} & \cdots & a_{t+\tau,t+\tau} \end{pmatrix} \quad (5)$$

where the first  $t$  rows are the coefficients corresponding to the EEG channels, the last  $\tau$  rows are the coefficients corresponding to the reference EMG channels, the coefficients in each column represent the weights of this IC to all EEG/EMG channels.

To develop an automatic method of identifying and rejecting the independent components related to EMG artifacts (referred to as ‘‘artifact ICs’’) in real EEG data after running ICA, two criteria were defined:

- First, a threshold was established based on the root mean square (RMS) values of coefficients in the mixing matrix rows corresponding to the EMG channels, which was defined as:

$$R_{ms} = \frac{\sum(\sqrt{\frac{\sum_{n=1}^{t+\tau} a_{t+1,n}^2}{t+\tau}} + \dots + \sqrt{\frac{\sum_{n=1}^{t+\tau} a_{t+\tau,n}^2}{t+\tau}})}{\tau} \quad (6)$$

where  $R_{ms}$  denotes the RMS value of coefficients. The true threshold was calculated by RMS value times gain. Gain is a constant which was empirically set between 0.4–3. *The ICs whose absolute value of coefficients in the corresponding EMG rows were above the threshold were defined to be artifact ICs.*

- Second, the ICs whose maximal absolute value of coefficients ( $\max(|a_{1,i}|, \dots, |a_{t+\tau,i}|)$ ,  $1 \leq i \leq (t + \tau)$ ) corresponds to a hat band electrode, were rejected. Note that hat band electrodes were defined as all the EEG electrodes which were on the outermost circumference of the head, as defined by [62] (Supplementary Fig. 8).

In order to find the proper threshold, we changed the gain set with 0.1 intervals so that a threshold set was limited to 0.4–3 times RMS value. The threshold was automatically set at the value which simultaneously minimizes high-frequency band (40 – 100 Hz) synchronization for all the EEG channels and maximizes  $\mu$  (8 – 12 Hz) desynchronization in the EEG channel of interest (e.g. C3/C4 for hand movements). Specifically, the threshold was decided automatically by finding the minimal value from the summated high-frequency band synchronization and  $\mu$  band desynchronization vector (an example of finding the proper gain was shown in Fig. 2).

## 2.2. Validation with Simulated EEG/EMG Data

To mathematically verify ERASE, simulated EMG and EEG were generated, subjected to ERASE, and its performance was assessed by several metrics as follows. Here, simulated EMG was also used as reference EMG artifacts for the experimental data processing.

*2.2.1. Generating simulated EMG* The simulated EMG was generated as the contaminant and reference EMG artifacts, using the approach below [63]:

- (i) The Hodgkin-Huxley model was used to simulate extracellular current. For skeletal muscles, the Hodgkin-Huxley model is a widely accepted model for simulating extracellular current [64].
- (ii) Single fiber action potentials (SFAP) were generated with a volume conduction model, defined as follows [65]:

$$V_E(z, y) = K \left\{ \int_{S_1} \frac{\partial e(z)}{\partial z} \cdot \frac{1}{r} dS + \int_S dS \int_{-\infty}^{+\infty} \frac{\partial^2 e(z)}{\partial z^2} \cdot \frac{1}{r} dz - \int_{S_2} \frac{\partial e(z)}{\partial z} \cdot \frac{1}{r} dS \right\} \quad (7)$$

where  $V_E$  is the SFAP,  $e(z)$  is the extracellular current (from step 1 above),  $z$  and  $y$  are the axial and radial directions, respectively,  $S_1$  and  $S_2$  are the fiber sections

at the fiber ends, and  $r$  is the distance between the surface element, and  $dS$  is the observation point. The equation above was discretized to generate the SFAP using known parameter values from the literature, including fiber length, endplate position, observation position, etc. [1, 66].

- (iii) A Gaussian distribution with 0 mean and standard deviation (SD) = 2.5 mm [66] was used to depict the endplate positions. The voltage propagation velocities were considered as a Gaussian distribution with an average of 4 m/s and SD = 0.125 [66]. A total of 100 SFAPs were first generated and their average served as one activation of the motor unit action potential (MUAP).
- (iv) A Poisson process was employed to model the firing rate of the MUAPs (as defined in [66]). The EMG firing rate and amplitude were assumed to increase with the hand/finger movements. Hence, different firing rates were applied to different phases (idle vs movement). For each muscle, the new Poisson process with the same firing rate was launched to generate the time points of the firing of MUAP.
- (v) Eight different facial muscles, including bilateral frontalis, temporalis, masseter, and trapezius were simulated for each session (one session denoted one record, which included several trials). Each muscle’s simulated EMG was filtered based on its frequency characteristics as described in the literature [1].

The above approach ensured that the simulated reference EMG was dependent on the contaminant EMG artifacts to some degree. Therefore, the effectiveness in removing EMG artifacts by using the simulated EMG should be similar with that obtained by using the real EMG.

These simulated EMG artifacts were then combined with the simulated EEG data (as described below) as separate channels (the “EMG channels”). These separate channels were located at different positions on the edge of brain topographic map (Supplementary Fig. 8). The coordinates of these positions corresponded to the approximate muscle locations on the head.

*2.2.2. Generating simulated EEG* Simulated EEG data was generated by using the approach in [67]:

- (i) Simulated EEG was created using a linear mixture of five Gaussian noises. Each Gaussian noise was bandpass filtered in different frequency bands (1-30 Hz, 20-40 Hz, 40-80 Hz, 80-100 Hz, and 100-200 Hz). The amplitude and variance of each Gaussian noise were adjusted to fit the average values of real EEG data.
- (ii) To mimic the spatial correlation between EEG channels due to volume conduction, a smoothing convolution was performed across channels to increase the spatial correlation amongst adjacent channels. The smoothing convolution kernel was a Gaussian function with a standard deviation equal to 4 channels. We considered the last channels on the list were correlated with the first channels on the list. Note that this resulted in consecutive channels being highly correlated (i.e. channel 1 becomes highly correlated to channel 2, channel 2 to 3, etc).



Simulated EEG data sets were generated with a temporal structure similar to real EEG. More specifically, each simulated dataset contained 32 channels, the maximal amplitude was set to  $60 \mu\text{V}$  with a variance of  $30 \mu\text{V}^2$ , and the sampling rate was set to 2000 Hz. A total of 5 minutes of simulated EEG was generated. Theoretically, the number of EEG channels (still meet the minimum for ICA run) has no effect on our approach, so we can select any number of EEG channels as long as we feel it is appropriate.

*2.2.3. Performance Assessment* The performance of ERASE was assessed in two simulated scenarios. In Scenario 1, ERASE was tested across an increasing number of contaminated EEG channels. Here, 3 types of simulated EMG (frontalis, temporalis, and masseter) were generated (as in Section 2.2.1). In the first iteration, 200 sets of simulated EEG (32 channels) were generated (6 channels were contaminated). Specifically, pairs of simulated EEG channels were then contaminated by a single simulated EMG type, and this was repeated until all 3 types were exhausted. Simulated EMG was multiplied by a randomly generated weight factor and added to the simulated EEG. For each simulated EMG, 2 normally distributed pseudorandom numbers were generated (mean: 0 and standard deviation: 1) and normalized to act as weight factors. Subsequently, the simulated EMG without multiplication was combined with the contaminated EEG set as separate channels. This combined dataset was subjected to ICA. This process was repeated with 12, 18, 24, and 30 simulated EEG channels, in which groups of 4, 6, 8, and 10 simulated EEG channels, respectively, were contaminated with a single EMG type.

For Scenario 2, ERASE was tested on simulated EEG across an increasing burden of EMG contamination. Here, 1 set of simulated EMG was generated for each of the following types: frontalis, temporalis, masseter, trapezius, and eye blinks (as in Section 2.2.1). Also, 200 sets of simulated EEG were generated as described above. For each set of simulated EEG, 6 randomly chosen simulated EEG channels were contaminated by a single EMG type. More specifically, the simulated EMG was multiplied by a randomly generated weight factor and then added to the simulated EEG. For each simulated EMG, 6 normally distributed pseudorandom numbers were generated (mean: 0 and standard deviation: 1) and normalized to act as weight factors. Likewise, the simulated EMG without multiplication were combined with the contaminated set of EEG as separate channels, thereby acting as reference EMG artifacts (e.g. there were 32 EEG channels, the simulated EMG was the 33rd, 34th,...37th channel, depending on how many simulated EMG channels were used). This combined dataset was subjected to ICA. This process was repeated, each time incrementally adding another simulated EMG type to an additional 6 randomly chosen simulated EEG channels, until all EMG types were exhausted. Note that to simplify the process, one simulated EEG channel was contaminated with no more than one type of simulated EMG in both scenarios.

Each combined simulated EEG/EMG set was then subjected to the ICA algorithm (FastICA). The performance was assessed by calculating the effectiveness, false positive

rate and sensitivity (described below) across all of the above data sets. Note that when using simulated EEG (Section 2.2.2), a threshold was not necessary to define artifact ICs. Instead, for each reference EMG channel, the IC with the highest coefficient was defined as an artifact IC.

**Effectiveness:** To compare how well EMG artifacts were removed between ERASE and the conventional ICA, the effectiveness of both methods were compared. Here, effectiveness was defined as the ratio of the amount of simulated EEG signal in the artifact ICs. Effectiveness was expressed as artifact index, which was defined as the following:

$$AI = \frac{\sum(|a_i^*| + \dots + |a_{i+j}^*|)/j}{\sum(|a_1| + \dots + |a_{i-1}| + |a_{i+j+1}| + \dots + |a_{32}|)/(32 - j)} \quad (8)$$

where  $a$  and  $a^*$  are defined in equation (9). Equation (8) denotes the ratio of the average mixing matrix coefficient values in the contaminated rows and those in the uncontaminated rows in the artifacts IC columns (referred to equation (9)). A larger artifact index indicated that this identified artifact IC contained more artifacts, but less simulated EEG signal.

We applied ERASE to two conditions of EMG-artifacts contaminated simulated EEG: with and without separate channels. Generally, we referred to this latter case as “conventional ICA” condition. The artifact indices calculated for the conditions with and without simulated EMG were statistically compared in order to verify the effectiveness of our model. Note that only criteria 2 from the rejection criteria above was employed in the conventional ICA condition.

**False positive rate:** To determine how frequently ERASE would erroneously detect sources that were independent of the reference EMG artifacts, a false positive rate was designed. More specifically, false positive rate determined how often contaminant artifacts ( $N_t$ , equation 1) that were *independent of* the reference EMG artifacts ( $n_\tau^*$ , equation 1) were erroneously “pushed” into the artifact ICs. To assess this,  $N_t$ , composed of Gaussian random noise (mean 0, S.D. 30), was used to further contaminate the simulated EEG. Simulated EMG was still used as reference EMG artifacts,  $n_\tau^*$ , and combined with the contaminated EEG data sets and acted as separate channels as described above. To simplify the process, only one type of (independent) Gaussian random artifacts was employed for both scenarios.

Here, we define the mixing matrix column corresponding to the artifact IC (the “artifact IC column”) as follows:

$$V = (a_1, \dots, a_{i-1}, a_i^*, \dots, a_{i+j}^*, a_{i+j+1}, \dots, a_{32}, \tilde{a}_{33}, \dots, \tilde{a}_{36})^T (1 \leq i \leq 26, 6 \leq i + j \leq 32) \quad (9)$$

where  $V$  is the “artifact IC column”,  $a$  denotes the coefficients corresponding to uncontaminated channels (the “non-artifacts coefficients”),  $a^*$  denotes the coefficients corresponding to contaminated channels (“artifacts coefficients”),  $\tilde{a}$  denotes the coefficients corresponding to the EMG channels,  $i$  and  $j$  are the number of uncontaminated channels and contaminated channels, respectively. Given that the ICs were normalized to unit variance, the coefficients contained in a given column

of the mixing matrix (equation 5) can be interpreted as relative loads by which this IC contributed to the mixed signals. Therefore, in the artifact IC columns, large coefficient values are usually associated with the channels that were contaminated by artifacts, whereas uncontaminated channels would have relatively smaller coefficients. Satisfying this inequality (10) meant that the corresponding artifacts were detected in these artifact ICs. After running ERASE on the combined simulated EEG data sets, all the artifact ICs, which were decided by the position of the maximal absolute values in the corresponding mixing matrix rows representing the EMG channels, were found. A false positive was formally defined as:

$$\sum (|a_i^*| + \dots + |a_{i+j}^*|) / j - \sum (|a_1| + \dots + |a_{i-1}| + \dots + |a_{i+j+1}| + \dots + |a_{32}|) / (32 - j) > \max(|\tilde{a}_{33}|, \dots, |\tilde{a}_{36}|) * 5\% \quad (10)$$

where  $\max(|\tilde{a}_{33}|, \dots, |\tilde{a}_{36}|)$  is defined as the maximal artifacts coefficient. If this inequality was satisfied in any artifact ICs, i.e. contaminated channels coefficients exceeded those for the uncontaminated channels by 5% of the maximal artifacts coefficient (denoted as the threshold in Fig. 1), a false positive event occurred. The ratio of those false positive events in 200 simulated data sets was the false positive rate.

**Sensitivity:** A sensitivity was designed to assess if contaminant EMG artifacts  $N_t$  were accurately “pushed” into the artifact ICs, when contaminant EMG artifacts,  $N_t$ , were *dependent on* reference EMG artifacts  $n_r^*$ . Sensitivity was defined as the ratio of events in which the contaminant EMG artifacts  $N_t$  were detected in the artifact ICs after running ERASE. The simulated EMG which served as both contaminant EMG artifacts and reference EMG artifacts here, were used to contaminate the simulated EEG data as described above and also acted as separate channels. These combined simulated EEG data sets were subjected to ICA. Referring to the artifact ICs columns, the sensitivity in our study was calculated by the ratio of events in which the inequality (10) was satisfied in all the artifact ICs columns in corresponding 200 simulated data sets.

### 2.3. Validation with real EEG

The ability of ERASE to automatically reject real EMG artifacts from real EEG was assessed as follows.

**2.3.1. Experiments** This study was approved by the Institutional Review Boards of the University of California, Irvine. Healthy subjects with no history of neurological conditions were recruited for this study. Subjects were fitted with a 64-channel EEG cap (ActiCap, Brain Products, Gilching, Germany) and asked to perform repetitive fist clenching and unclenching of the dominant hand while their EEG signals were acquired by two, linked NeXus-32 systems (Mind Media, Herten, Netherlands). EMG was recorded from the bilateral frontalis, left temporalis to masseter, right temporalis to masseter and bilateral trapezius using a MP150 system (BIOPAC, Goleta CA), respectively. The subjects were asked to sit in front of a computer screen, which prompted them to alternate between idling (for 5 s) or hand fist-clenching (for 2 s).

This was repeated for a total of 10 trials over a 100s-long session. At least 2 sessions were performed by each subject. The EEG and EMG data were recorded at 2048 Hz and 4000 Hz sampling rates, respectively.

*2.3.2. Experimental data processing* For the experimental EEG, both real and simulated EMG artifacts acted as separate channels and were not mixed to any EEG channels. The combined EEG/EMG data were bandpass filtered from 3 to 100 Hz (3<sup>rd</sup> order, forward-backward filter with no phase distortion). Note that the 100 Hz upper cutoff was chosen since the amplifiers attached to MP150 have a 100 Hz low-pass filter in hardware. Each trial, comprised 1-s idle time followed by 2-s movement, was identified and extracted from the combined EEG. Due to the non-stationarity of EEG, ICA decomposition was just applied to concatenated EEG trial datasets for each session (each run). The FastICA version in the EEGLAB toolbox [68] was used to run ICA on the EEG trials data for all the subjects in the three conditions (simulated EMG, real EMG, and conventional ICA conditions). The artifact ICs were rejected as above. Short-time Fourier transform was applied to EEG trials and the signal power in different frequency bands ( $\mu$  band: 8 to 12 Hz, high frequency (HF) band: 40 to 100 Hz) was compared across all ICA conditions. All the data were z-scored after the time-frequency decomposition, which were separately normalized to the statistics of the EEG during the idling epochs.

The z-scored power of the  $\mu$  and high-frequency bands during idle and movement was statistically compared for all the EEG channels using a Wilcoxon rank-sum test. The z-scored power of  $\mu$ /high-frequency band for each channel was then topographically mapped. For channels where there was no significant difference between idle and movement, these values were nulled (set to 0).

Given that the absolute power at any frequency bands was reduced after artifact ICs were rejected from the original signal, we used the z-scored power of high-frequency band to calculate the decrease of high frequency after removal of EMG artifacts for each subject. The percent reduction was defined as below:

$$PD = \frac{|\sum_{c=1}^C \sum_{i=1}^N P_z^b(X_i^c) - \sum_{c=1}^C \sum_{i=1}^N P_z^a(X_i^c)|}{\sum_{c=1}^C \sum_{i=1}^N P_z^b(X_i^c)} \times 100\% \quad (11)$$

where  $P_z^b$  is the z-scored power of high frequency in baseline,  $P_z^a$  is the z-scored power of high frequency after removal of EMG artifacts,  $X$  are the EEG trials data,  $i$  is the  $i^{th}$  trial,  $N$  is the total number of available trials for each subject,  $c$  is the  $c^{th}$  channel,  $C$  is the total number of EEG channels. The rationale for this approach is that the high-frequency signal is dominated by EMG in EEG and any reduction in the high-frequency band power was considered as the reduction in EMG. The Wilcoxon rank-sum test was also employed to examine the difference of the  $\mu$  band power in the C3/C4 channel and the high-frequency band power in all of the channels during movement between all combinations of the 4 conditions (baseline, after ERASE with simulated EMG, after ERASE with real EMG, and after conventional ICA).

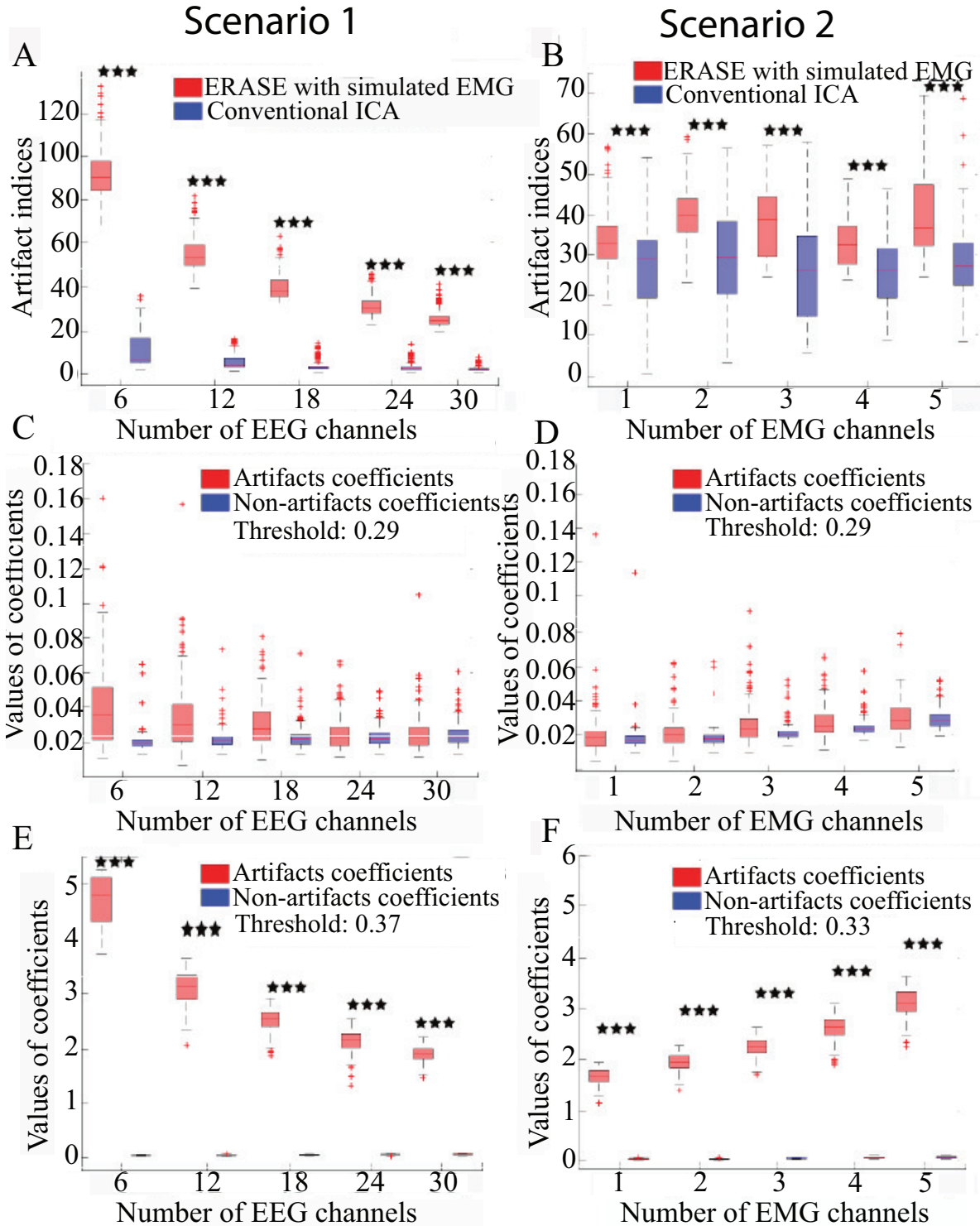


**Figure 1.** Effectiveness, false positive, and sensitivity of ERASE on the simulated data. **A**, **B**. Artifact indices, i.e., effectiveness in Scenario 1, 2 respectively. **C**, **D**. False positive for Scenario 1 and 2, respectively. **E**, **F**. Sensitivity results for Scenario 1 and 2, respectively. Scenario 1 was considered as the fact that the number of contaminated EEG was changed for the performance assessment of ERASE. Here, the number of contaminated EEG channels were chosen from 2 to 10 for each simulated EMG artifacts (three EMG artifacts were used here, so numbers are 6 to 30 in figures). We increased the number of added EMG channels in Scenario 2 for the performance assessment of ERASE. The number of added EMG channel was chosen from 1 to 5. Asterisks indicate a significant difference between two data sets (Wilcoxon Rank-Sum Test), and the significance level=\*\*\* $p < 0.001$ .

### 3. RESULTS

#### 3.1. Simulation verification

- a. **Effectiveness:** The artifact indices for ERASE and conventional ICA were summarized in Fig. 1 A and B. Across all parameters, the artifact indices calculated by equation 8 in ERASE were significantly larger than those in the conventional ICA model (Wilcoxon rank-sum test,  $P < 0.001$ ). This indicates that ERASE has better effectiveness in removing the EMG artifacts compared to the conventional ICA model.
- b. **False Positive Rate:** The artifacts and non-artifacts coefficients for the false positive were summarized in Fig. 1 C and D. Across all parameters, there was a 0% rate of false positive, as defined by Inequality 10 (details regarding thresholds are in Supplementary Table 1). Furthermore, the values of artifacts and non-artifacts coefficients were small and were not significantly different from one another. This indicates that signals independent of the reference artifacts were not erroneously “pushed” into artifact ICs by ERASE.
- c. **Sensitivity:** The artifacts and non-artifacts coefficients for the sensitivity were summarized in Fig. 1 E and F. Across all parameters, there was a 100% rate of sensitivity, as defined by Equation 10 (details about threshold were shown in Supplementary Table 2). Furthermore, the values of artifacts and non-artifacts coefficients were significantly different from one another (Wilcoxon rank-sum test,  $P < 0.001$ ) and the values of non-artifacts coefficients were always significantly lower. This indicates that contaminant EMG artifacts can be accurately identified by ERASE.

#### 3.2. Experimental Verification

A total of 8 subjects gave their informed consent to participate in the study. All subjects were healthy male volunteers between 20 and 50 years old. A total of 12 sessions (120 trials) were performed across all subjects.

An example of selecting the proper threshold for ERASE was shown in Fig. 2. Table 1 summarized the effect of ERASE on the  $\mu$ -band and high-frequency band across all subjects. Overall, the high-frequency band power, typically dominated by EMG artifacts, was reduced by 75.31% using ERASE with real EMG, by 63.46% through ERASE with simulated EMG and only by 48.88% with the conventional ICA approach (Table 1). At the group level (Fig. 3 A), the z-scored power of the high-frequency band during movement was significantly reduced after running ERASE. Furthermore, the high-frequency band power in the real EMG and simulated EMG conditions were both significantly lower than that in the conventional ICA (Fig. 3 A). However, there was no difference between running ERASE with either the real EMG or simulated EMG. At the group level, there was no change in the  $\mu$  band (only for C3/C4 channel) among the

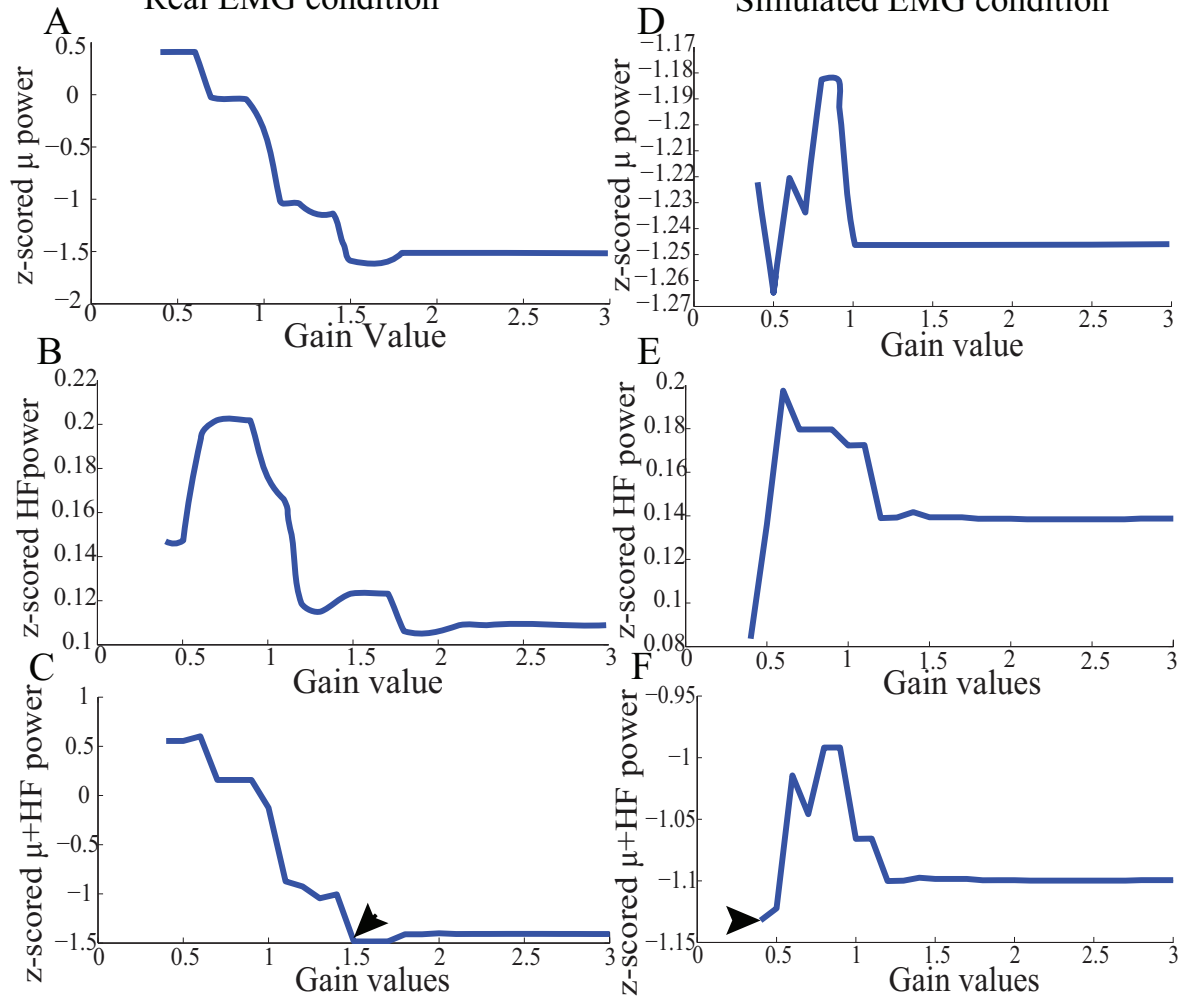


**Figure 2.** Representative z-scored  $\mu$  and high-frequency band power from Subject 1 after running ICA (as in Section 2.3.2), using simulated EMG and real EMG. **A.** Average of z-scored  $\mu$  power in the C3 channel in the real EMG condition. **B.** Average of z-scored high-frequency band power for all the EEG channels in the real EMG condition. **C.** Values added by z-scored high-frequency band and  $\mu$  power in the real EMG condition. **D.** Average of z-scored  $\mu$  power in the C3 channel in the simulated EMG condition. **E.** Average of z-scored high-frequency band power for all the EEG channels in the simulated EMG condition. **F.** Values added by z-scored high-frequency band and  $\mu$  power in the simulated EMG condition. After running ICA on the combined EEG/EMG data, the artifact ICs were rejected based on the criteria depicted above for each threshold. After the joint consideration, the final threshold was 1.5 for real EMG condition, and 0.4 for simulated EMG, which were denoted by arrows.

four conditions based on all trials (Fig. 3 B). This indicates that the expected  $\mu$ -band desynchronization phenomenon during the fist-clenching task was not adversely affected by ICA.

A representative example of significant changes in z-scored power of  $\mu$  and high-frequency bands during idle and movement is shown in Fig. 4. The z-scored power of high-frequency band during movement was reduced after running ERASE, and the power in both ERASE conditions was smaller than that in the conventional ICA

**Table 1.** Change of HF band power in different conditions for each subject ( mean  $\pm$  standard deviation (S.D))

Subject	S1	S2	S3	S4*	S5	S6	S7	S8*
<b>Baseline</b>								
Z-scored HF band	0.35 $\pm$ 0.26	0.18 $\pm$ 0.14	0.35 $\pm$ 0.24	0.24 $\pm$ 0.163	0.04 $\pm$ 0.04	0.18 $\pm$ 0.13	0.50 $\pm$ 0.19	0.71 $\pm$ 0.25
Z-scored $\mu$ band	-0.86 $\pm$ 0.58	-0.13 $\pm$ 0.04	-0.01 $\pm$ 0.07	-0.91 $\pm$ 0.58	-0.48 $\pm$ 0.18	-0.97 $\pm$ 0.72	-0.57 $\pm$ 0.49	0.04 $\pm$ 0.32
<b>After ERASE with real EMG</b>								
Z-scored HF band	0.12 $\pm$ 0.06	0.06 $\pm$ 0.07	0.03 $\pm$ 0.02	0.11 $\pm$ 0.06	0.40 $\times 10^{-4}$ $\pm 0.01$	0.02 $\pm 0.30$ $\times 10^{-2}$	0.10 $\pm$ 0.08	0.31 $\pm$ 0.03
Z-scored $\mu$ band	-0.78 $\pm$ 0.38	-0.43 $\pm$ 0.18	-0.40 $\pm$ 0.25	-1.03 $\pm$ 0.39	-0.48 $\pm$ 0.26	-1.03 $\pm$ 0.48	-0.67 $\pm$ 0.18	-0.82 $\pm$ 0.56
Reduction percentage (%)	64.42	67	90.96	54.19	99	91.4	79.94	55.57
<b>After ERASE with simulated EMG</b>								
Z-scored HF band	0.12 $\pm$ 0.16	0.08 $\pm$ 0.08	0.06 $\pm$ 0.06	0.12 $\pm$ 0.10	0.50 $\times 10^{-4}$ $\pm 0.50 \times 10^{-2}$	0.03 $\pm$ 0.08	0.15 $\pm$ 0.08	0.31 $\pm$ 0.12
Z-scored $\mu$ band	-0.92 $\pm$ 0.44	-0.31 $\pm$ 0.24	-0.32 $\pm$ 0.13	-0.90 $\pm$ 0.49	-0.33 $\pm$ 0.34	-0.90 $\pm$ 0.59	-0.50 $\pm$ 0.12	-0.84 $\pm$ 0.35
Reduction percentage (%)	65.77	56.16	83.62	50	99	83.08	69.79	56.45
<b>Conventional ICA</b>								
Z-scored HF band	0.17 $\pm$ 0.14	0.09 $\pm$ 0.07	0.17 $\pm$ 0.11	0.17 $\pm$ 0.12	0.70 $\times 10^{-2}$ $\pm 0.8 \times 10^{-2}$	0.08 $\pm$ 0.01	0.19 $\pm$ 0.09	0.41 $\pm$ 0.13
Z-scored $\mu$ band	-0.57 $\pm$ 0.72	-0.21 $\pm$ 0.35	0.10 $\pm$ 0.12	-0.58 $\pm$ 0.35	-0.39 $\pm$ 0.29	-0.58 $\pm$ 0.72	-0.50 $\pm$ 0.17	-0.70 $\pm$ 0.30
Reduction percentage (%)	51.8	52.96	52.54	26.76	82.06	56.99	61.92	41.99

HF: high frequency.

z-scored HF band: the average z-scored power during movement over all the available sessions.

Reduction percentage: the difference between high-frequency band power in baseline and after ERASE or conventional ICA was divided by high-frequency band power in the baseline.

Twenty trials were employed for calculation for Subject 4 and 8 (denoted by asterisks). Ten trials were used for the remaining subjects.

(Fig. 4 E-H, Supplementary Fig. 1-7 E-H. A representative example of time series also showed the same findings (Supplementary Fig. 9)). In Fig. 4 A-D, the  $\mu$  desynchronization during right hand movement was well preserved after running ICA in all the conditions and was localized to the C3 channel and surrounding electrodes. This localized  $\mu$  desynchronization was also present around the C3 channel for Subjects 3 to 7 (Supplementary Fig. 1-5 A-D) and around the C4 channels for Subjects 2 and 8 (Supplementary Fig. 6-7 A-D). The channels exhibiting  $\mu$  desynchronization were always contralateral to the hand movement except Subjects 2 and 8 (Supplementary Figs.1 and 7). Combined with the findings above, this indicates that ERASE did not disturb the spatial distribution of the expected brain features underlying the motor task of interest.

#### 4. Discussion

Here, we proposed a modified ICA model that combined reference EMG artifacts with EEG data to facilitate an enhanced automated removal of EMG artifacts. We tested and validated this method using both simulated and actual EEG during hand movement. We found that it had high sensitivity at detecting EMG artifacts and an extremely low false positive rate (Fig. 1 C-F, Supplementary Table 1 and 2). With simulated data, ERASE effectively removed a large proportion of the EMG artifacts (Fig. 1 A-B). It also removed EMG artifacts in real EEG recordings, while preserving the expected  $\mu$  desynchronization associated with movement (Fig. 4 and Supplementary Figs. 1-7). This may also indicate that our approach can remove any potential confounding overlap between EMG and EEG and thereby improves the confidence that low-frequency brain



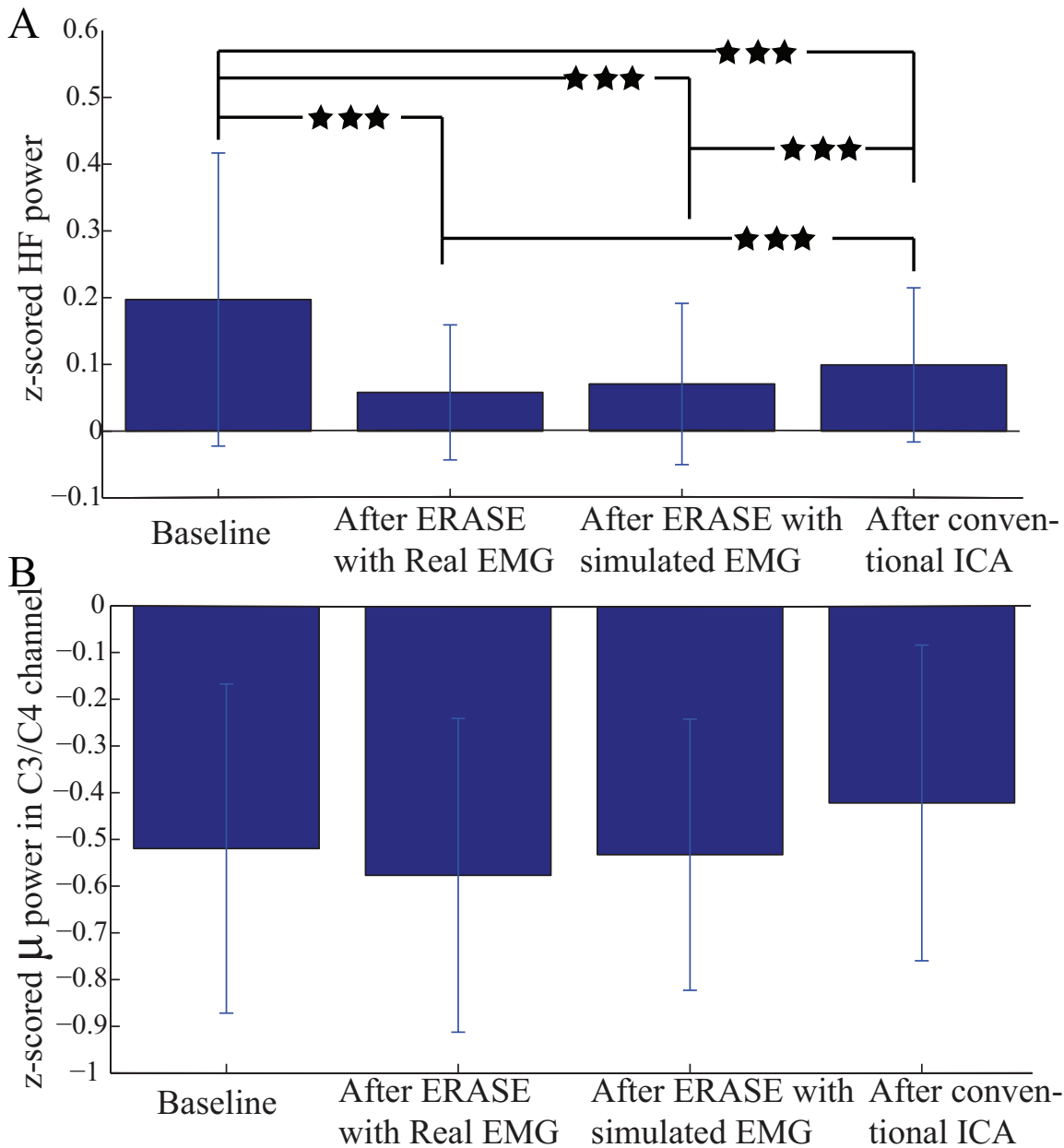


**Figure 3.** Comparison of z-scored power of  $\mu$ /high-frequency band during movement in different conditions. **A.** z-scored power of high-frequency band during the movement for all the EEG channels under different conditions. **B.** z-scored power of  $\mu$  band during movement in the C3/C4 channel under different conditions. Data were from all the subjects with a total of 120 trials. \*\*\*: significant differences between the two datasets ( $p < 0.001$ ).

features extracted from ERASE are mostly EMG-free (which cannot be achieved by a simple low pass filter).

These results suggest that using reference EMG artifacts can force ICA to “learn” and detect the EMG artifacts by forcing the contaminant EMG within EEG into a minimal number of ICs. We established an operational definition (rejection criteria) for identifying EMG artifacts components to enable automated component rejection

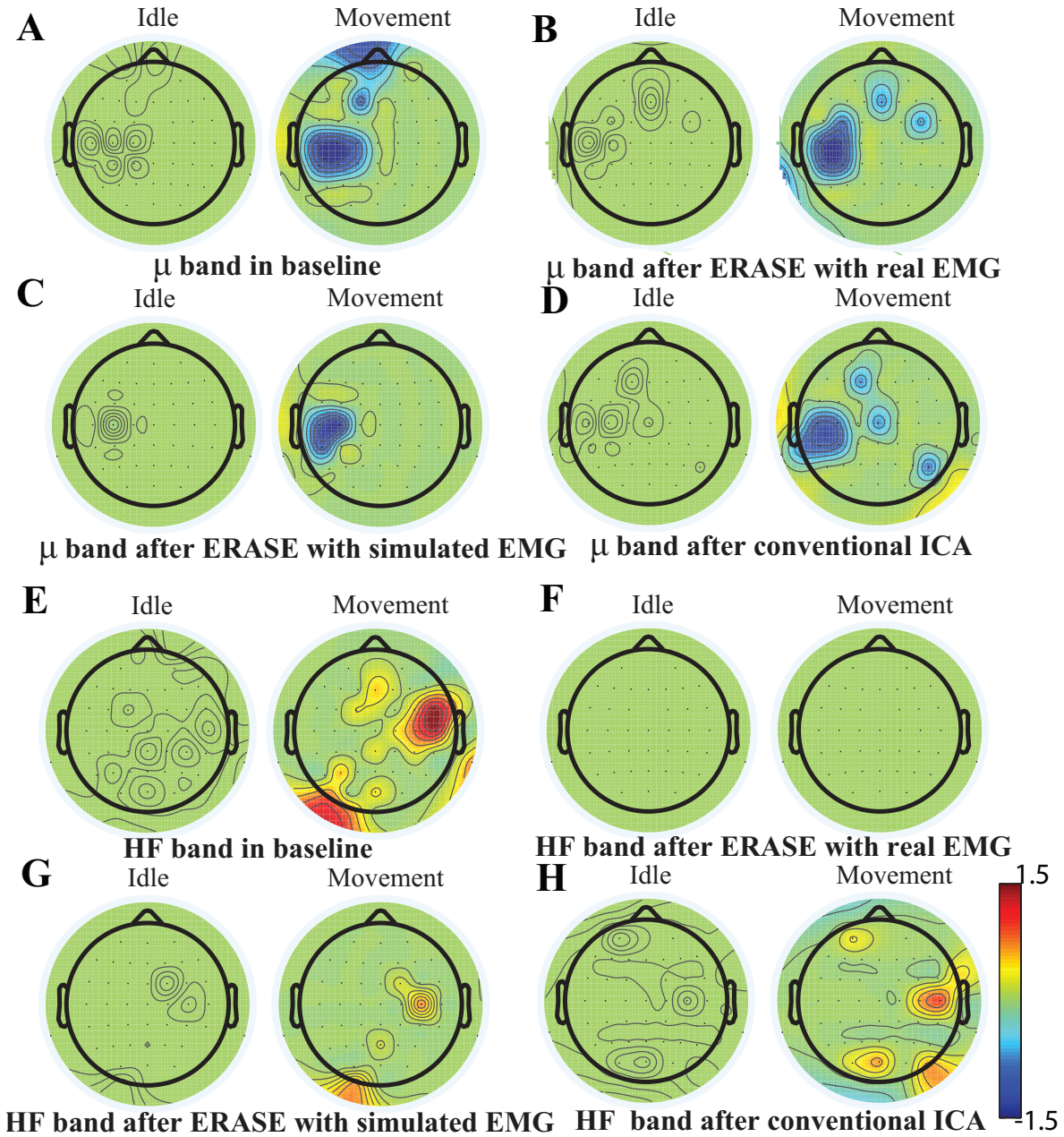


**Figure 4.** Brain topography maps for Subject 1 displaying the z-scored power of  $\mu$  band and high-frequency band in different conditions (baseline, after ERASE with real EMG and with simulated EMG and after conventional ICA, **A-D** for  $\mu$  band and **E-H** for high-frequency band) on the Subject 1. Channels whose z-scored power of  $\mu$ /high-frequency band were not significantly different between idle and movement states (Wilcoxon rank-sum test) were nulled (values were set to zero). The significance threshold was  $P < 0.01$  for  $\mu$  band and  $P < 0.05$  for high-frequency band.

and thereby minimizing user bias. Compared to conventional ICA, results showed that ERASE removed on average 26% more EMG artifacts from EEG data than conventional ICA (Fig. 3 and Table 1), which indicated that ERASE improved the ICA algorithm. Although this approach may require slightly more preparation time to record real EMG, it is still possible to use it in situations where real EMG recordings were either

not possible or not available by substituting it with simulated EMG (Fig. 3). The advantages and novelty of this approach are discussed in further detail below.

First, ERASE directly introduces reference EMG artifacts into the ICA model as prior knowledge to more accurately maximize the separation between EMG and EEG ICs as well as to minimize the computational complexity of removing EMG with respect to existing cICA approaches. On the other hand, previously reported forms of reference ICA, such as spatially cICA [56, 57], involves first performing an initial run of ICA on a previous EEG data segment, followed by manually selecting ICs believed to represent EMG sources as EMG reference. Subsequently, ICA is run iteratively on current EEG data to find all the ICs which have a strong correlation with pre-defined EMG reference. By comparison, ERASE real EMG (where available) or simulated EMG as the reference. Since such references are expected to provide a more reliable representation of the ground truth for EMG sources, ERASE is likely more reliable and systematic than other forms of ICA. In addition, ERASE utilizes properties of mixing matrix for identification of artifact ICs to avoid the complicated computation of optimization problem, which is employed in temporally cICA [13, 54, 55]. When combined with the use of a simulated or simultaneously recorded real EMG used in ERASE, it is not necessary to perform iterative run for the ICA process. Our results (Figs. 3 and 4 and Table 1) showed that ERASE can remove most of EMG artifacts and preserve expected brain features just after a single ICA run.

Unlike previously reported versions of ICA, ERASE does not require manual intervention. More specifically, ICA is typically run directly on EEG, and the operator manually rejects the artifact ICs. The effectiveness of this step depends substantially on the experience of researchers and may be biased due to subjectivity. Hence, ERASE can minimize the biases of researchers and improve the efficiency of artifacts rejection. As mentioned in the introduction, automated rejection is not necessarily unique to ERASE [14, 16, 46, 47, 59, 60, 69–71], given that other methods, such as cICA can also involve automatic IC rejection when prior knowledge of EMG signals is available [3, 56, 57]. However, one unique aspect of ERASE compared to these prior reports is that rejection criteria are based on physiological features of both EEG and EMG for automated EMG artifacts rejection procedure (Section 2.1.2), which makes ERASE more focused on preserving relevant EEG phenomenon.

ERASE was validated with both simulated and behavioral EEG data, whereas the physiological information and properties of EEG are completely overlooked in other EMG artifact removal studies using ICA, cICA, or other BSS methods. Researchers typically employ simulated or synthetic EEG data to validate corresponding artifacts removal algorithms. Based on various metrics (discussed in the paragraph below), all of these algorithms have declared themselves effective at removing EMG artifacts, but have not answered a critical question as to whether the information encoded in EEG is retained after artifact removal. Here, we show that EEG  $\mu$  band modulation that typically underlies hand movement is preserved or even enhanced after ERASE. Combined with the reduction of EMG elsewhere in the EEG, these findings

unequivocally demonstrate that meaningful EEG is retained. Such a demonstration has been generally absent from the validation of other ICA approaches.

It should be noted that ICA was selected as the basis of ERASE due to the fact that ICA has typically been shown to have superior performance to most other artifact removal methods. For example, CCA, a popular algorithm for artifact removal, does not outperform ICA at removing EMG artifacts from EEG [3, 17, 39, 40] as well as at removing ECG and EOG artifacts [41–46]. Some BSS methods and source decomposition methods have been combined for removal of EMG artifacts (e.g. EEMD-CCA [19, 38, 73], as well as EEMD-ICA [28]). Both EMD and EEMD are single-channel techniques, so EEMD-CCA and EEMD-ICA are only tested on the fact that a few channels of EEG recording are involved. Since running ICA or CCA sometimes is time-consuming, EEMD-CCA or EEMD-ICA probably is typically less than ideal.

There are no uniformly accepted performance metrics for artifacts removal algorithm in practical EEG. In most studies [79–81], the performance of EMG artifact removal is typically assessed, in part, by visual inspection. Although highly subjective, it may give an indication with respect to whether the algorithm has improved the quality of the EEG signal or has distorted one or more time intervals or frequency bands. This is also performed in our study and the results are showed in Supplementary Fig. 9. For simulated and synthetic EEG, there are many metrics employed for the assessment of the performance of artifact removal approaches, since the ‘ground truth’ in such scenarios are explicitly known [17, 28, 57, 82–84]. The most widely used metrics for performance assessment are listed in the literature [3] (e.g. the relative root mean squared error (RRMSE), the signal to artifact ratio (SAR), etc.). In our work, we used standard statistical metrics (false positive, sensitivity, effectiveness) to validate our approach in simulated EEG. Meanwhile, time-series validation results are shown in Supplementary Figs. 10-12 in the Appendix. It should also be emphasized that since researchers in each study used different data sets, a head-to-head performance comparison across various artifact removal approaches in EEG studies is difficult. Therefore, we further validated our novel approach by using an assessing both the elimination of EMG and the preservation of the EEG features underlying motor behaviors. We propose that such an evaluation is employed for validation of effectiveness of any new artifact rejection approaches in future studies, as it is otherwise not possible to know if the methodology aggressively removed EMG as well as erroneously eliminating the signals of interest.

The main limitations of ERASE are that it is still impossible to remove all EMG from EEG. The main reason originates from the assumptions of our theoretical model. Namely, our model requires that the reference EMG artifacts and contaminant EMG artifacts are completely dependent. However, contaminant EMG artifacts in EEG data cannot have complete dependence on the real EMG sources due to several reasons. For example, the signal propagation path between the true source and recording electrodes may significantly distort observed EMG. It is also not possible to include all the reference EMG artifacts which could be contributing to EEG, because some head and neck muscles are not easily recorded at the surface. In addition, another assumption in

our theoretical derivation is that the reference EMG artifacts are independent of EEG. Also, the reference EMG electrodes are close to potential EEG sources (such as EMG reference electrodes located over the frontalis and temporalis muscles), so it is difficult to ensure that the reference EMG artifacts channels in this study are fully independent of EEG. Hence, the identified artifact ICs may still contain some contribution from EEG. However, EEG from these areas is not highly involved in motor tasks in our studies.

## 5. CONCLUSION

Here, we proposed a modified ICA model that can automatically remove EMG artifacts by combining reference EMG artifacts with EEG. This new approach can more effectively remove EMG artifacts from EEG while preserving the expected brain features underlying motor behavior. Also, the approach proposed in this work is automated, which minimizes experimenter bias and speeds up analysis. The utilization of the simulated EMG as the reference EMG source potentially extends the application of this approach. The EEG recovered by our approach can provide more confidence for further neuroscience analysis. Meanwhile, future work will focus on testing ERASE on EEG from patient populations, and adapting it for real-time applications, such as in the BCI system.

## 6. Appendix

Appendix: We showed the results of z-scored power of  $\mu$  band (8 to 12 Hz) and high frequency band (40 to 100 Hz) in different conditions (baseline, after ERASE with real EMG and simulated EMG and after conventional ICA) for Subject 2-8 (Figs. 1-7), the 2D image of the electrode locations (Fig. 8), time series band-pass filtered with 40-100 Hz for one trial in different conditions (Fig. 9), time series validation results by using simulated EEG with simulated EMG (Fig. 10) and real EMG (Fig. 11), and performance comparison between ERASE and conventional ICA by a common metric. Also, Table 1 and 2 list the average thresholds for false positive and sensitivity test, respectively. Table 3 lists the average artifact indices for the simulated EMG and conventional ICA conditions.

## References

- [1] Suresh Muthukumaraswamy. High-frequency brain activity and muscle artifacts in meg/eeg: a review and recommendations. *Frontiers in human neuroscience*, 7:138, 2013.
- [2] Mehrdad Fatourech, Ali Bashashati, Rabab K Ward, and Gary E Birch. Emg and eeg artifacts in brain computer interface systems: A survey. *Clinical neurophysiology*, 118(3):480–494, 2007.

- [3] Jose Antonio Urigüen and Begoña Garcia-Zapirain. Eeg artifact removal state-of-the-art and guidelines. *Journal of neural engineering*, 12(3):031001, 2015.
- [4] Jesus Minguillon, M Angel Lopez-Gordo, and Francisco Pelayo. Trends in eeg-bci for daily-life: Requirements for artifact removal. *Biomedical Signal Processing and Control*, 31:407–418, 2017.
- [5] Kevin T Sweeney, Tomás E Ward, and Seán F McLoone. Artifact removal in physiological signals practices and possibilities. *IEEE transactions on information technology in biomedicine*, 16(3):488–500, 2012.
- [6] Carlos Guerrero-Mosquera and Angel Navia Vazquez. Automatic removal of ocular artifacts from eeg data using adaptive filtering and independent component analysis. In *2009 17th European Signal Processing Conference*, pages 2317–2321. IEEE, 2009.
- [7] Fabio Morbidi, Andrea Garulli, Domenico Prattichizzo, Cristiano Rizzo, Paolo Manganotti, and Simone Rossi. Off-line removal of tms-induced artifacts on human electroencephalography by kalman filter. *Journal of neuroscience methods*, 162(1-2):293–302, 2007.
- [8] Gabriele Gratton, Michael GH Coles, and Emanuel Donchin. A new method for off-line removal of ocular artifact. *Electroencephalography and clinical neurophysiology*, 55(4):468–484, 1983.
- [9] Maarten De Vos, Katharina Gandras, and Stefan Debener. Towards a truly mobile auditory brain–computer interface: exploring the p300 to take away. *International journal of psychophysiology*, 91(1):46–53, 2014.
- [10] Joseph T Gwin, Klaus Gramann, Scott Makeig, and Daniel P Ferris. Removal of movement artifact from high-density eeg recorded during walking and running. *Journal of neurophysiology*, 103(6):3526–3534, 2010.
- [11] P Berg and M Scherg. Dipole modelling of eye activity and its application to the removal of eye artefacts from the eeg and meg. *Clinical Physics and Physiological Measurement*, 12(A):49, 1991.
- [12] Nicole Ille, Patrick Berg, and Michael Scherg. Artifact correction of the ongoing eeg using spatial filters based on artifact and brain signal topographies. *Journal of clinical neurophysiology*, 19(2):113–124, 2002.
- [13] Christopher J James and Christian W Hesse. Independent component analysis for biomedical signals. *Physiological measurement*, 26(1):R15, 2004.
- [14] Hugh Nolan, Robert Whelan, and Richard B Reilly. Faster: fully automated statistical thresholding for eeg artifact rejection. *Journal of neuroscience methods*, 192(1):152–162, 2010.
- [15] Pierre Comon. Independent component analysis, a new concept? *Signal processing*, 36(3):287–314, 1994.
- [16] Andrea Mognon, Jorge Jovicich, Lorenzo Bruzzone, and Marco Buiatti. Adjust:

- An automatic eeg artifact detector based on the joint use of spatial and temporal features. *Psychophysiology*, 48(2):229–240, 2011.
- [17] Doha Safieddine, Amar Kachenoura, Laurent Albera, Gwénaél Birot, Ahmad Karfoul, Anca Pasnicu, Arnaud Biraben, Fabrice Wendling, Lotfi Senhadji, and Isabelle Merlet. Removal of muscle artifact from eeg data: comparison between stochastic (ica and cca) and deterministic (emd and wavelet-based) approaches. *EURASIP Journal on Advances in Signal Processing*, 2012(1):127, 2012.
- [18] Md Rakibul Mowla, Siew-Cheok Ng, Muhammad SA Zilany, and Raveendran Paramesran. Artifacts-matched blind source separation and wavelet transform for multichannel eeg denoising. *Biomedical Signal Processing and Control*, 22:111–118, 2015.
- [19] Xun Chen, Aiping Liu, Joyce Chiang, Z Jane Wang, Martin J McKeown, and Rabab K Ward. Removing muscle artifacts from eeg data: Multichannel or single-channel techniques? *IEEE Sensors Journal*, 16(7):1986–1997, 2015.
- [20] Kevin T Sweeney, Seán F McLoone, and Tomas E Ward. The use of ensemble empirical mode decomposition with canonical correlation analysis as a novel artifact removal technique. *IEEE transactions on biomedical engineering*, 60(1):97–105, 2012.
- [21] Rémi Gribonval and Sylvain Lesage. A survey of sparse component analysis for blind source separation: principles, perspectives, and new challenges. 2006.
- [22] Ana R Teixeira, Ana Maria Tomé, Elmar Wolfgang Lang, Peter Gruber, and A Martins Da Silva. Automatic removal of high-amplitude artefacts from single-channel electroencephalograms. *Computer methods and programs in biomedicine*, 83(2):125–138, 2006.
- [23] David L Donoho and Iain M Johnstone. Adapting to unknown smoothness via wavelet shrinkage. *Journal of the american statistical association*, 90(432):1200–1224, 1995.
- [24] Michael Unser and Akram Aldroubi. A review of wavelets in biomedical applications. *Proceedings of the IEEE*, 84(4):626–638, 1996.
- [25] Hong Peng, Bin Hu, Qiuxia Shi, Martyn Ratcliffe, Qinglin Zhao, Yanbing Qi, and Guoping Gao. Removal of ocular artifacts in eegan improved approach combining dwt and anc for portable applications. *IEEE journal of biomedical and health informatics*, 17(3):600–607, 2013.
- [26] Nasser Mourad and Rami K Niazy. Automatic correction of eye blink artifact in single channel eeg recording using emd and omp. In *21st European Signal Processing Conference (EUSIPCO 2013)*, pages 1–5. IEEE, 2013.
- [27] Hong Zeng, Aiguo Song, Ruqiang Yan, and Hongyun Qin. Eog artifact correction from eeg recording using stationary subspace analysis and empirical mode decomposition. *Sensors*, 13(11):14839–14859, 2013.

- [28] Bogdan Mijovic, Maarten De Vos, Ivan Gligorijevic, Joachim Taelman, and Sabine Van Huffel. Source separation from single-channel recordings by combining empirical-mode decomposition and independent component analysis. *IEEE transactions on biomedical engineering*, 57(9):2188–2196, 2010.
- [29] Tatjana Zikov, Stephane Bibian, Guy A Dumont, Mihai Huzmezan, and CR Ries. A wavelet based de-noising technique for ocular artifact correction of the electroencephalogram. In *Proceedings of the Second Joint 24th Annual Conference and the Annual Fall Meeting of the Biomedical Engineering Society [Engineering in Medicine and Biology]*, volume 1, pages 98–105. IEEE, 2002.
- [30] V Krishnaveni, S Jayaraman, L Anitha, and K Ramadoss. Removal of ocular artifacts from eeg using adaptive thresholding of wavelet coefficients. *Journal of Neural Engineering*, 3(4):338, 2006.
- [31] Zhaohua Wu and Norden E Huang. Ensemble empirical mode decomposition: a noise-assisted data analysis method. *Advances in adaptive data analysis*, 1(01):1–41, 2009.
- [32] Xun Chen, Chen He, and Hu Peng. Removal of muscle artifacts from single-channel eeg based on ensemble empirical mode decomposition and multiset canonical correlation analysis. *Journal of Applied Mathematics*, 2014, 2014.
- [33] Xun Chen, Aiping Liu, Hu Peng, and Rabab Ward. A preliminary study of muscular artifact cancellation in single-channel eeg. *Sensors*, 14(10):18370–18389, 2014.
- [34] Hoang-Anh T Nguyen, John Musson, Feng Li, Wei Wang, Guangfan Zhang, Roger Xu, Carl Richey, Tom Schnell, Frederic D McKenzie, and Jiang Li. Eog artifact removal using a wavelet neural network. *Neurocomputing*, 97:374–389, 2012.
- [35] Christiaan Burger and David Jacobus van den Heever. Removal of eeg artefacts by combining wavelet neural network and independent component analysis. *Biomedical Signal Processing and Control*, 15:67–79, 2015.
- [36] Jing Hu, Chun-sheng Wang, Min Wu, Yu-xiao Du, Yong He, and Jinhua She. Removal of eeg and emg artifacts from eeg using combination of functional link neural network and adaptive neural fuzzy inference system. *Neurocomputing*, 151:278–287, 2015.
- [37] S Suja Priyadharsini, S Edward Rajan, and S Femilin Sheniha. A novel approach for the elimination of artefacts from eeg signals employing an improved artificial immune system algorithm. *Journal of Experimental & Theoretical Artificial Intelligence*, 28(1-2):239–259, 2016.
- [38] Xun Chen, Xueyuan Xu, Aiping Liu, Martin J McKeown, and Z Jane Wang. The use of multivariate emd and cca for denoising muscle artifacts from few-channel eeg recordings. *IEEE transactions on instrumentation and measurement*, 67(2):359–370, 2017.
- [39] Brenton W McMenamin, Alexander J Shackman, Jeffrey S Maxwell, David RW Bachhuber, Adam M Koppenhaver, Lawrence L Greischar, and Richard J Davidson.



- Validation of ica-based myogenic artifact correction for scalp and source-localized eeg. *Neuroimage*, 49(3):2416–2432, 2010.
- [40] Javier Escudero, Roberto Hornero, Daniel Abásolo, and Alberto Fernández. Quantitative evaluation of artifact removal in real magnetoencephalogram signals with blind source separation. *Annals of biomedical engineering*, 39(8):2274–2286, 2011.
- [41] Sergio Romero, Miguel A Mañanas, and Manel J Barbanoj. A comparative study of automatic techniques for ocular artifact reduction in spontaneous eeg signals based on clinical target variables: a simulation case. *Computers in biology and medicine*, 38(3):348–360, 2008.
- [42] S Romero, MA Mañanas, and Manel J Barbanoj. Ocular reduction in eeg signals based on adaptive filtering, regression and blind source separation. *Annals of biomedical engineering*, 37(1):176–191, 2009.
- [43] Arnaud Delorme, Jason Palmer, Julie Onton, Robert Oostenveld, and Scott Makeig. Independent eeg sources are dipolar. *PloS one*, 7(2):e30135, 2012.
- [44] Ian D Evans, Graham Jamieson, Rodney Croft, and Trieu T Pham. Empirically validating fully automated eeg artifact correction using independent components analysis. In *ACNS-2012 Australasian Cognitive Neuroscience Conference*, 2012.
- [45] Trieu TH Pham, Rodney J Croft, Peter J Cadusch, and Robert J Barry. A test of four eeg correction methods using an improved validation technique. *International Journal of Psychophysiology*, 79(2):203–210, 2011.
- [46] Ian Daly, Nicoletta Nicolaou, Slawomir Jaroslaw Nasuto, and Kevin Warwick. Automated artifact removal from the electroencephalogram: A comparative study. *Clinical EEG and Neuroscience*, 44(4):291–306, 2013.
- [47] Arnaud Delorme, Terrence Sejnowski, and Scott Makeig. Enhanced detection of artifacts in eeg data using higher-order statistics and independent component analysis. *Neuroimage*, 34(4):1443–1449, 2007.
- [48] Yvonne Tran, A Craig, P Boord, and D Craig. Using independent component analysis to remove artifact from electroencephalographic measured during stuttered speech. *Medical and Biological Engineering and Computing*, 42(5):627–633, 2004.
- [49] Alexander J Shackman, Brenton W McMenamin, Heleen A Slagter, Jeffrey S Maxwell, Lawrence L Greischar, and Richard J Davidson. Electromyogenic artifacts and electroencephalographic inferences. *Brain topography*, 22(1):7–12, 2009.
- [50] Sebastian Olbrich, Johannes Jödicke, Christian Sander, Hubertus Himmerich, and Ulrich Hegerl. Ica-based muscle artefact correction of eeg data: What is muscle and what is brain?: Comment on mcmenamin et al. *Neuroimage*, 54(1):1–3, 2011.
- [51] Joachim Gross, Sylvain Baillet, Gareth R Barnes, Richard N Henson, Arjan Hillebrand, Ole Jensen, Karim Jerbi, Vladimir Litvak, Burkhard Maess, Robert Oostenveld, et al. Good practice for conducting and reporting meg research. *Neuroimage*, 65:349–363, 2013.

- [52] Nadia Mammone, Fabio La Foresta, and Francesco Carlo Morabito. Automatic artifact rejection from multichannel scalp eeg by wavelet ica. *IEEE Sensors Journal*, 12(3):533–542, 2012.
- [53] Qiu-Hua Lin, Yong-Rui Zheng, Fu-Liang Yin, Hualou Liang, and Vince D Calhoun. A fast algorithm for one-unit ica-r. *Information Sciences*, 177(5):1265–1275, 2007.
- [54] Christopher J James and Oliver J Gibson. Temporally constrained ica: an application to artifact rejection in electromagnetic brain signal analysis. *IEEE Transactions on Biomedical Engineering*, 50(9):1108–1116, 2003.
- [55] Wei Lu and Jagath C Rajapakse. Approach and applications of constrained ica. *IEEE transactions on neural networks*, 16(1):203–212, 2005.
- [56] Christian W Hesse and Christopher J James. On semi-blind source separation using spatial constraints with applications in eeg analysis. *IEEE Transactions on Biomedical Engineering*, 53(12):2525–2534, 2006.
- [57] Muhammad Tahir Akhtar, Wataru Mitsuhashi, and Christopher J James. Employing spatially constrained ica and wavelet denoising, for automatic removal of artifacts from multichannel eeg data. *Signal processing*, 92(2):401–416, 2012.
- [58] Nicole Ille, Roland Beucker, and Michael Scherg. Spatially constrained independent component analysis for artifact correction in eeg and meg. *Neuroimage*, 6(13):159, 2001.
- [59] Ian Daly, Floriana Pichiorri, Josef Faller, Vera Kaiser, Alex Kreilinger, Reinhold Scherer, and Gernot Müller-Putz. What does clean eeg look like? In *2012 Annual International Conference of the IEEE Engineering in Medicine and Biology Society*, pages 3963–3966. IEEE, 2012.
- [60] Arnaud Delorme, Scott Makeig, and TJ Sejnowski. Automatic artifact rejection for eeg data using high-order statistics and independent component analysis. In *Proceedings of the third international ICA conference*, pages 9–12, 2001.
- [61] Garrick L Wallstrom, Robert E Kass, Anita Miller, Jeffrey F Cohn, and Nathan A Fox. Automatic correction of ocular artifacts in the eeg: a comparison of regression-based and component-based methods. *International journal of psychophysiology*, 53(2):105–119, 2004.
- [62] Thoru Yamada and Elizabeth Meng. *Practical guide for clinical neurophysiologic testing: EEG*. Lippincott Williams & Wilkins, 2012.
- [63] Yongcheng Li, Po T Wang, Mukta P Vaidya, Charles Y Liu, Marc W Slutzky, and An H Do. A novel algorithm for removing artifacts from eeg data. In *Engineering in Medicine and Biology Society, EMBC, 2018 Annual International Conference of the IEEE*. IEEE, 2018.
- [64] Alan L Hodgkin and Andrew F Huxley. A quantitative description of membrane current and its application to conduction and excitation in nerve. *The Journal of physiology*, 117(4):500–544, 1952.

- [65] Jacques Duchene and J-Y Hogrel. A model of emg generation. *IEEE transactions on biomedical engineering*, 47(2):192–201, 2000.
- [66] Dick F Stegeman and Wim HJP Linssen. Muscle fiber action potential changes and surface emg: A simulation study. *Journal of Electromyography and Kinesiology*, 2(3):130–140, 1992.
- [67] Frédéric Grouiller, Laurent Vercueil, Alexandre Krainik, Christoph Segebarth, Philippe Kahane, and Olivier David. A comparative study of different artefact removal algorithms for eeg signals acquired during functional mri. *Neuroimage*, 38(1):124–137, 2007.
- [68] Arnaud Delorme and Scott Makeig. Eeglab: an open source toolbox for analysis of single-trial eeg dynamics including independent component analysis. *Journal of neuroscience methods*, 134(1):9–21, 2004.
- [69] Nicoletta Nicolaou and Slawomir J Nasuto. Automatic artefact removal from event-related potentials via clustering. *The Journal of VLSI Signal Processing Systems for Signal, Image, and Video Technology*, 48(1-2):173–183, 2007.
- [70] Wei Wu, Corey J Keller, Nigel C Rogasch, Parker Longwell, Emmanuel Shpigel, Camarin E Rolle, and Amit Etkin. Artist: A fully automated artifact rejection algorithm for single-pulse tms-eeg data. *Human brain mapping*, 39(4):1607–1625, 2018.
- [71] Mukta Vaidya, Robert D Flint, Po T Wang, Alex Barry, Yongcheng Li, Mohammad Ghassemi, Goran Tomic, Jun Yao, Carolina Carmona, Emily M Mugler, et al. Hemispherectomy in traumatic brain injury: a noninvasive platform to investigate high gamma activity for brain machine interfaces. *IEEE Transactions on Neural Systems and Rehabilitation Engineering*, 2019.
- [72] Natalie Richer, Ryan J Downey, Andrew D Nordin, W David Hairston, and Daniel P Ferris. Adding neck muscle activity to a head phantom device to validate mobile eeg muscle and motion artifact removal. In *2019 9th International IEEE/EMBS Conference on Neural Engineering (NER)*, pages 275–278. IEEE, 2019.
- [73] Juan Andrés Mucarquer, Pavel Prado, María-José Escobar, Wael El-Deredy, and Matías Zañartu. Improving eeg muscle artifact removal with an emg array. *IEEE Transactions on Instrumentation and Measurement*, 2019.
- [74] Ricardo Vigário, Jaakko Sarela, V Jousmiki, Matti Hamalainen, and Erkki Oja. Independent component approach to the analysis of eeg and meg recordings. *IEEE transactions on biomedical engineering*, 47(5):589–593, 2000.
- [75] Akaysha Tang. Applications of second order blind identification to high-density eeg-based brain imaging: a review. In *International Symposium on Neural Networks*, pages 368–377. Springer, 2010.
- [76] Mark Girolami. An alternative perspective on adaptive independent component analysis algorithms. *Neural Computation*, 10(8):2103–2114, 1998.

- [77] Zhi-Qin John Xu, Fang Xu, Guoqiang Bi, Douglas Zhou, and David Cai. A cautionary tale of entropic criteria in assessing the validity of the maximum entropy principle. *EPL (Europhysics Letters)*, 126(3):38005, 2019.
- [78] Aapo Hyvärinen and Erkki Oja. Independent component analysis: algorithms and applications. *Neural networks*, 13(4-5):411–430, 2000.
- [79] De Maarten Vos, Stephanie Riès, Katrien Vanderperren, Bart Vanrumste, Francois-Xavier Alario, Van Sabine Huffel, and Boris Burle. Removal of muscle artifacts from eeg recordings of spoken language production. *Neuroinformatics*, 8(2):135–150, 2010.
- [80] Maite Crespo-Garcia, Mercedes Atienza, and Jose L Cantero. Muscle artifact removal from human sleep eeg by using independent component analysis. *Annals of biomedical engineering*, 36(3):467–475, 2008.
- [81] BRENTON W McMENAMIN, Alexander J Shackman, Jeffrey S Maxwell, Lawrence L Greischar, and Richard J Davidson. Validation of regression-based myogenic correction techniques for scalp and source-localized eeg. *Psychophysiology*, 46(3):578–592, 2009.
- [82] Laurent Albera, Amar Kachenoura, Pierre Comon, Ahmad Karfoul, Fabrice Wendling, Lotfi Senhadji, and Isabelle Merlet. Ica-based eeg denoising: a comparative analysis of fifteen methods. *Bulletin of the Polish Academy of Sciences: Technical Sciences*, 60(3):407–418, 2012.
- [83] Wim De Clercq, Anneleen Vergult, Bart Vanrumste, Wim Van Paesschen, and Sabine Van Huffel. Canonical correlation analysis applied to remove muscle artifacts from the electroencephalogram. *IEEE transactions on Biomedical Engineering*, 53(12):2583–2587, 2006.
- [84] C Zhang, J Yang, Y Lei, and F Ye. Single channel blind source separation by combining slope ensemble empirical mode decomposition and independent component analysis. *J. Comput. Inf. Syst*, 8(8):3117–3126, 2012.

## 7. Supplementary

## Part 1. Supplementary results

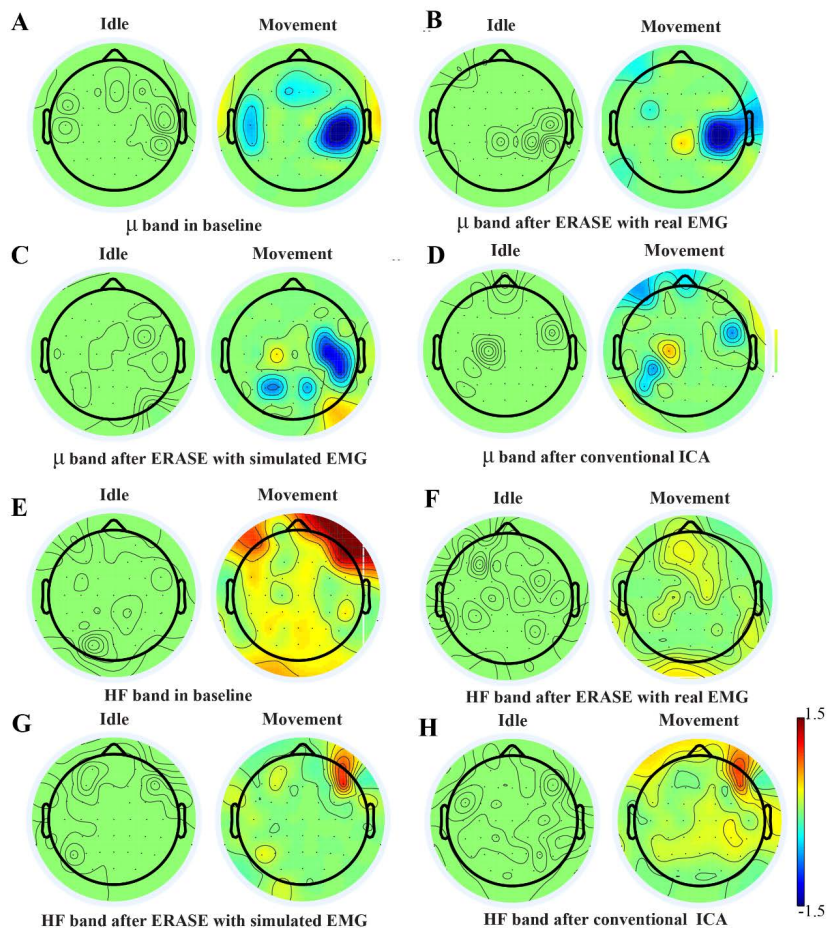


Fig. 1. Brain topography maps for Subject 2 displaying the power of  $\mu$  band (8 to 12 Hz) and high frequency band (40 to 100 Hz) in different conditions (baseline, after ERASE with real EMG condition and with simulated EMG and after conventional ICA), A-D for  $\mu$  band and E-H for high frequency band) on the Subject 2. Channels whose z-scored power of  $\mu$ /high frequency band were not significantly different between idle and movement states (Wilcoxon rank sum test) were nulled ( $P < 0.01$  for  $\mu$  band and 0.05 for high frequency band). The color bar is from -1.5 to 1.5.

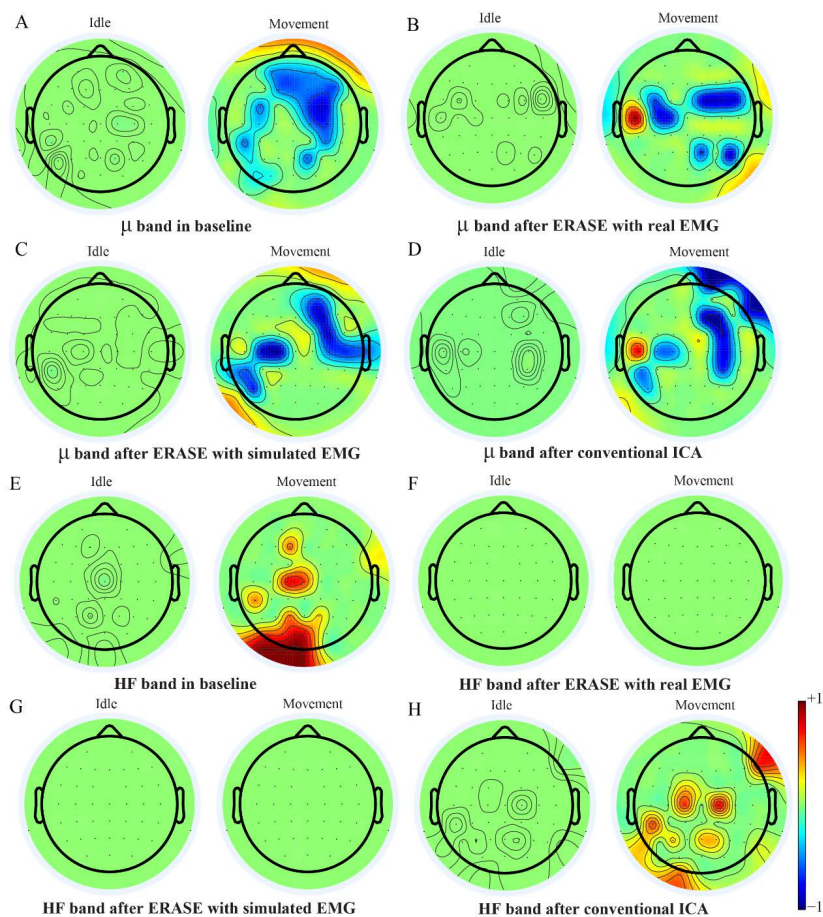


Fig. 2. Brain topography maps for Subject 3 displaying the power of  $\mu$  band (8 to 12 Hz) and high frequency band (40 to 100 Hz) in different conditions (baseline, after ERASE with real EMG condition and with simulated EMG and after conventional ICA), A-D for  $\mu$  band and E-H for high frequency band) on the Subject 3. Channels whose z-scored power of  $\mu$ /high frequency band were not significantly different between idle and movement states (Wilcoxon rank sum test) were nulled ( $P < 0.05$  for  $\mu$  band and 0.05 for high frequency band). The color bar is from -1 to 1.

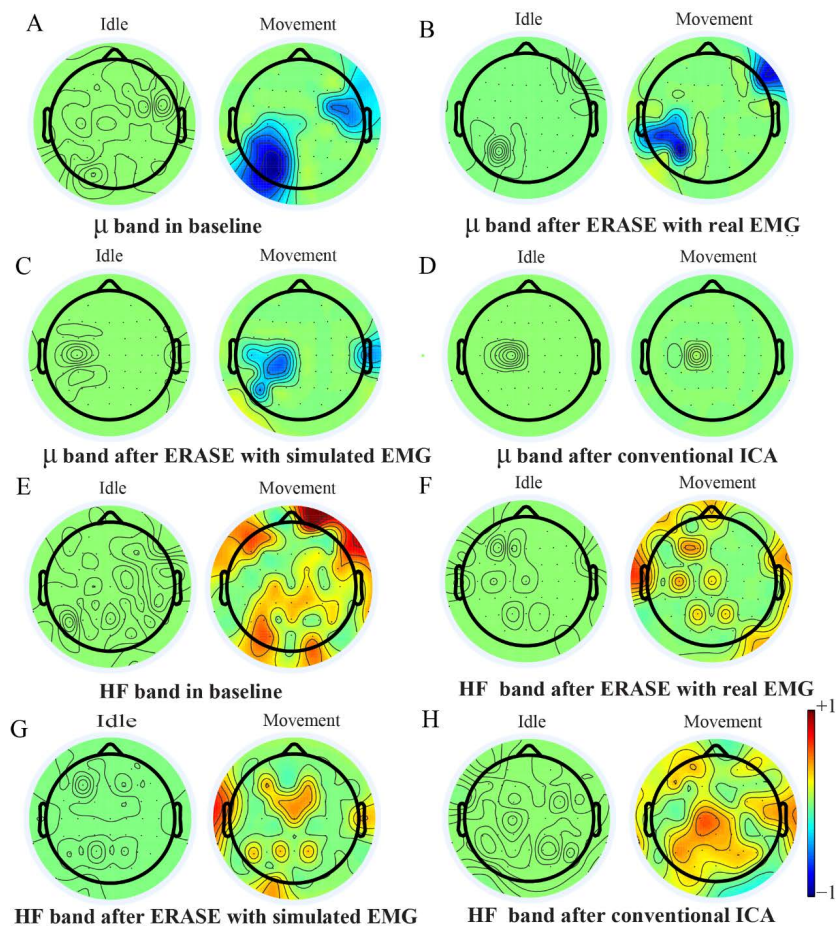


Fig. 3. Brain topography maps for Subject 4 displaying the power of  $\mu$  band (8 to 12 Hz) and high frequency band (40 to 100 Hz) in different conditions (baseline, after ERASE with real EMG condition and with simulated EMG and after conventional ICA), A-D for  $\mu$  band and E-H for high frequency band) on the Subject 4. Channels whose z-scored power of  $\mu$ /high frequency band were not significantly different between idle and movement states (Wilcoxon rank sum test) were nulled ( $P < 0.05$  for  $\mu$  band and 0.05 for high frequency band). The color bar is from -1 to 1.

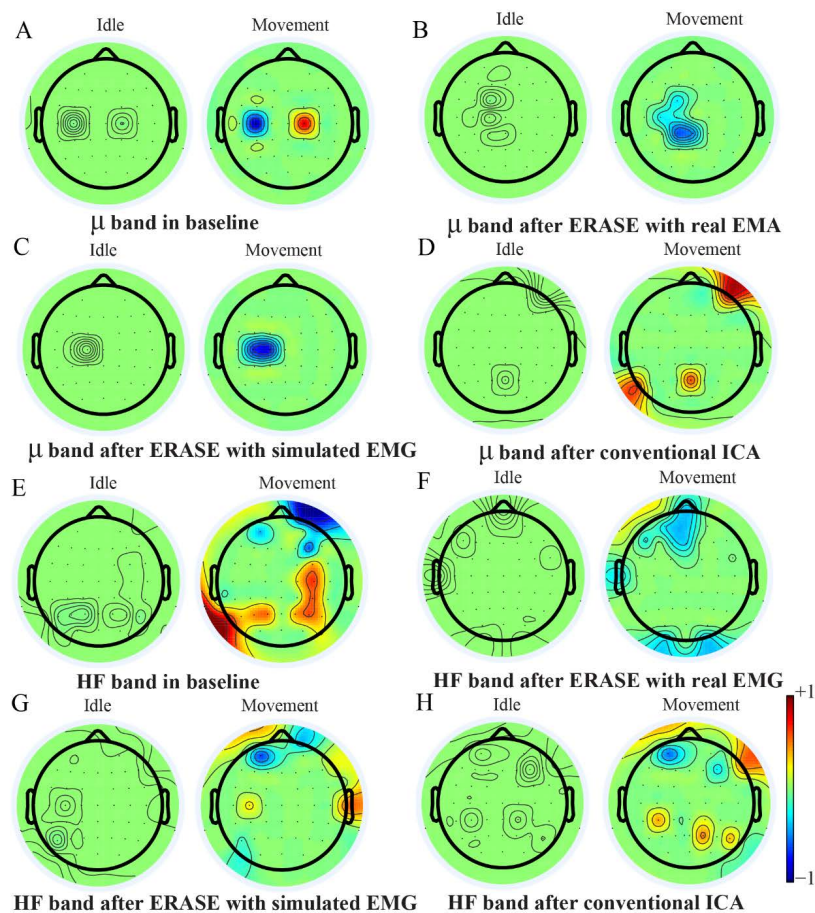


Fig. 4. Brain topography maps for Subject 5 displaying the power of  $\mu$  band (8 to 12 Hz) and high frequency band (40 to 100 Hz) in different conditions (baseline, after ERASE with real EMG condition and with simulated EMG and after conventional ICA), A-D for  $\mu$  band and E-H for high frequency band) on the Subject 5. Channels whose z-scored power of  $\mu$ /high frequency band were not significantly different between idle and movement states (Wilcoxon rank sum test) were nulled ( $P < 0.01$  for  $\mu$  band and 0.05 for high frequency band). The color bar is from -1 to 1.



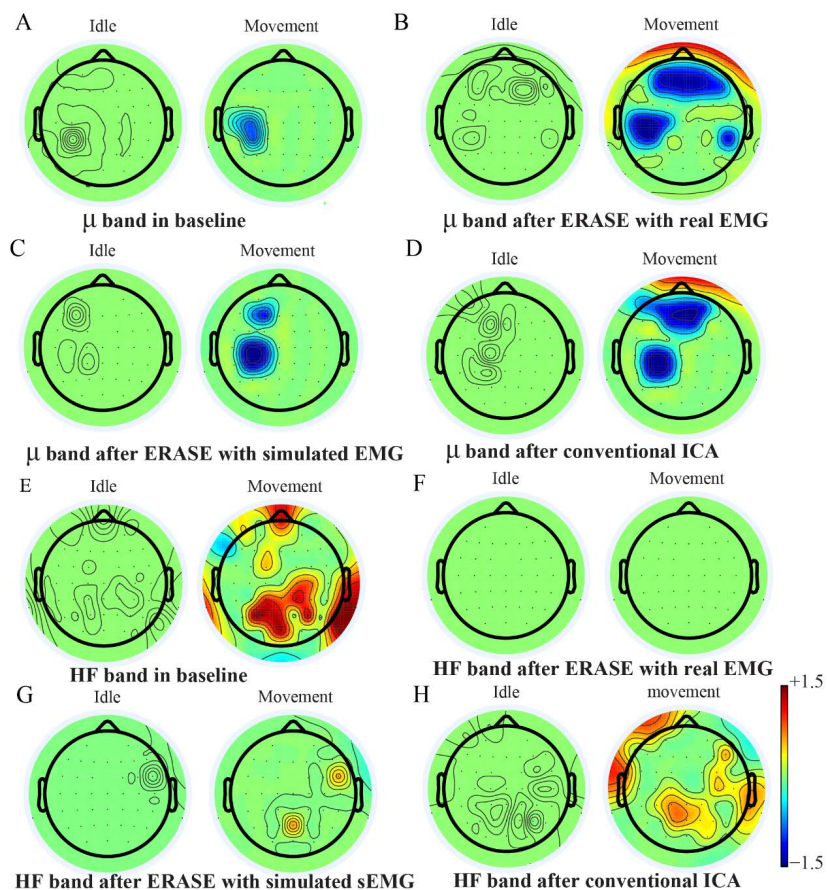


Fig. 5. Brain topography maps for Subject 6 displaying the power of  $\mu$  band (8 to 12 Hz) and high frequency band (40 to 100 Hz) in different conditions (baseline, after ERASE with real EMG condition and with simulated EMG and after conventional ICA), A-D for  $\mu$  band and E-H for high frequency band) on the Subject 6. Channels whose z-scored power of  $\mu$ /high frequency band were not significantly different between idle and movement states (Wilcoxon rank sum test) were nulled ( $P < 0.01$  for  $\mu$  band and 0.05 for high frequency band). The color bar is from -1.5 to 1.5.

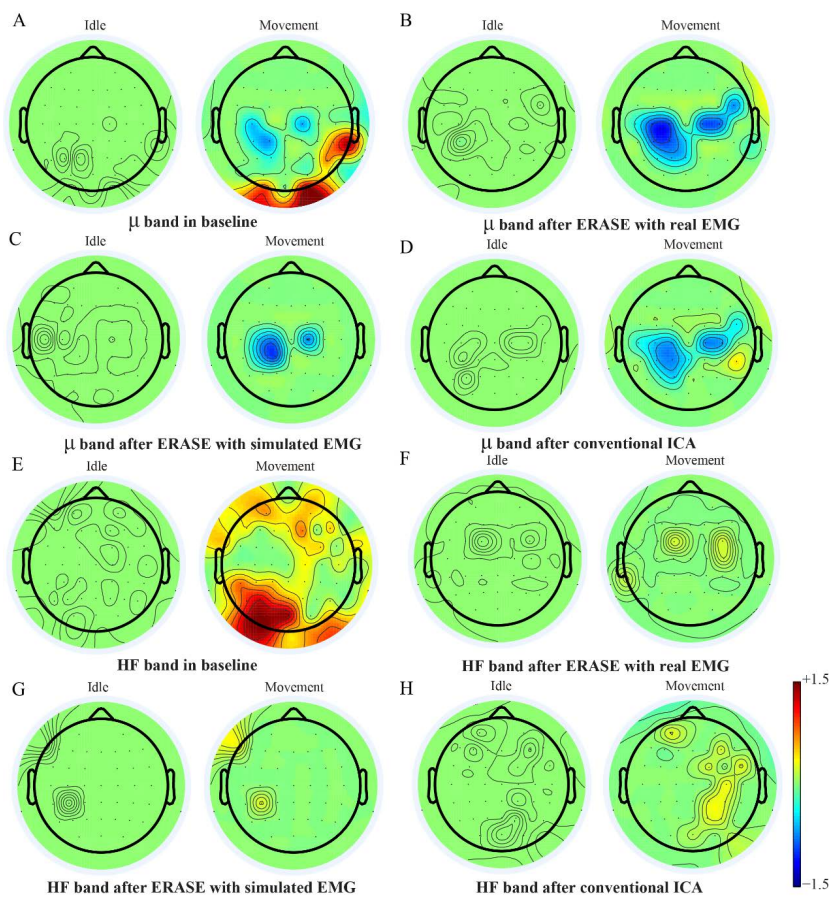


Fig. 6. Brain topography maps for Subject 7 displaying the power of  $\mu$  band (8 to 12 Hz) and high frequency band (40 to 100 Hz) in different conditions (baseline, after ERASE with real EMG condition and with simulated EMG and after conventional ICA), A-D for  $\mu$  band and E-H for high frequency band) on the Subject 7. Channels whose z-scored power of  $\mu$ /high frequency band were not significantly different between idle and movement states (Wilcoxon rank sum test) were nulled ( $P < 0.05$  for  $\mu$  band and 0.05 for high frequency band). The color bar is from -1.5 to 1.5.

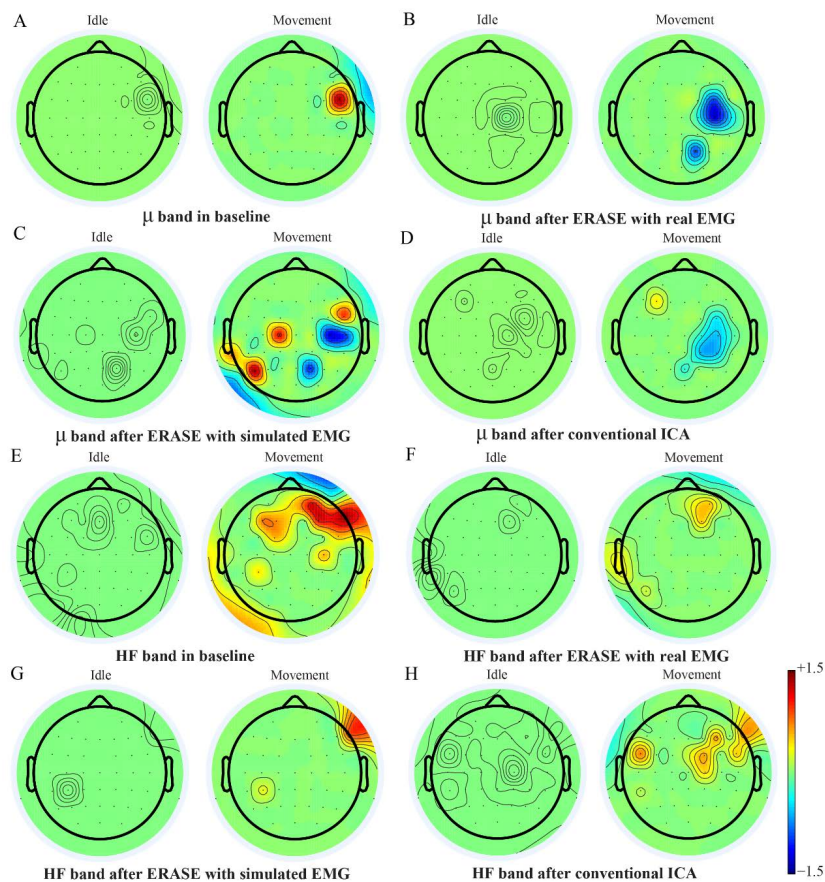


Fig. 7. Brain topography maps for Subject 8 displaying the power of  $\mu$  band (8 to 12 Hz) and high frequency band (40 to 100 Hz) in different conditions (baseline, after ERASE with real EMG condition and with simulated EMG and after conventional ICA), A-D for  $\mu$  band and E-H for high frequency band) on the Subject 8. Channels whose z-scored power of  $\mu$ /high frequency band were not significantly different between idle and movement states (Wilcoxon rank sum test) were nulled ( $P < 0.05$  for  $\mu$  band and 0.05 for high frequency band). The color bar is from -1.5 to 1.5.

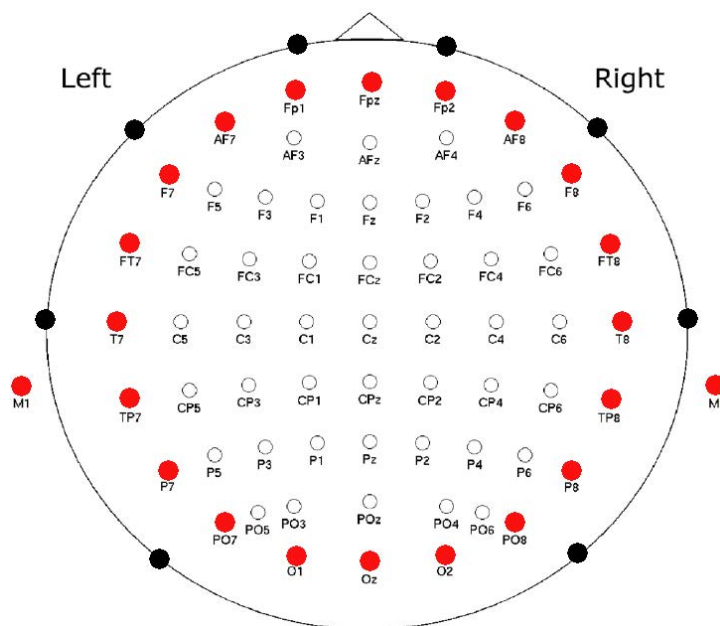


Figure 8. electrodes location of 64-channel cap. The red dots denote the hat band electrodes. The black dots outline the position of the added EMG channels.

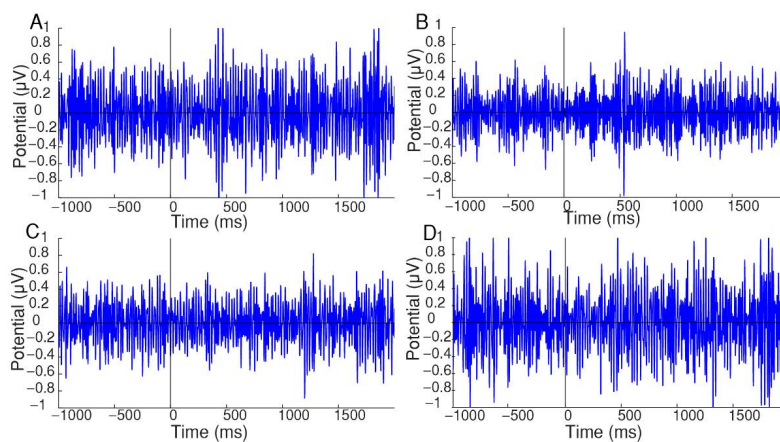


Figure 9. Time series band-pass filtered with frequency band from 40 Hz to 100Hz in different conditions (baseline, after ERASE with real EMG condition and with simulated EMG and after conventional ICA). Here, we show the data in one trial from C6 electrode. Data is from Subject 1. A. Time series baseline. B. Time series after ERASE with real EMG. B. Time series after ERASE with simulated EMG. B. Time series after conventional ICA.

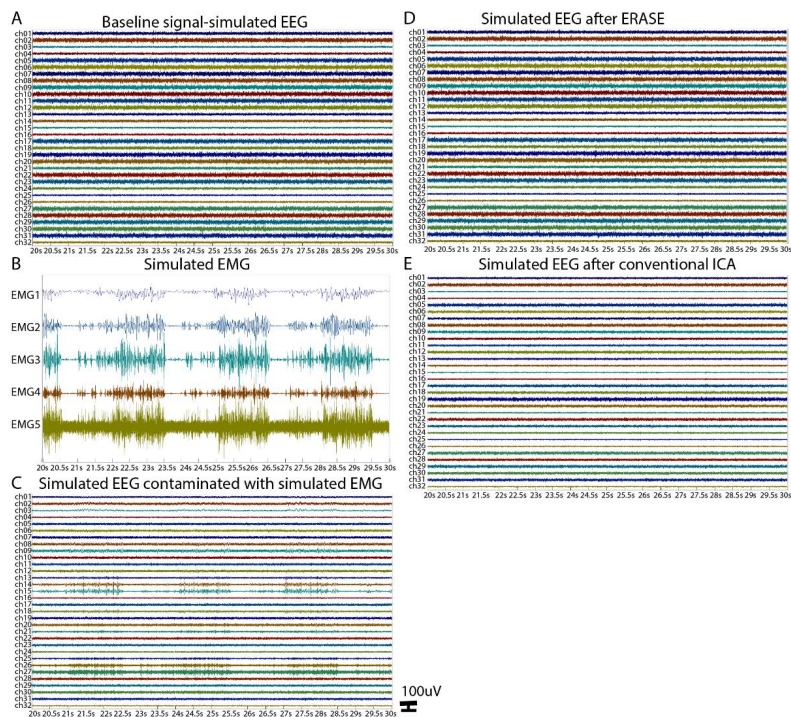


Figure 10. Sample of 10s time series. A. simulated EEG. B. simulated EMG. C. contaminated EEG signal (simulated EEG was contaminated by simulated EMG). In this example, SNR is 1. D. recovered EEG after running ERASE. E. recovered EEG after running conventional ICA.

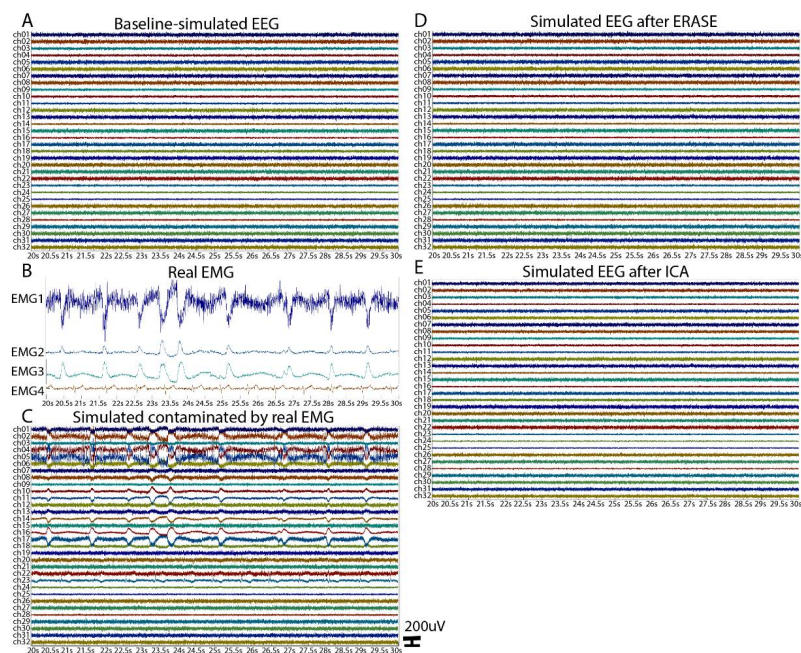


Figure 11. Sample of 10s time series. A. simulated EEG. B. real EMG. All real EMG in this figure was recorded from healthy subject (Subject 1). C. contaminated EEG signal (simulated EEG was contaminated by real EMG). In this example, SNR is 1. D. recovered EEG after running ERASE. E. recovered EEG after running conventional ICA.

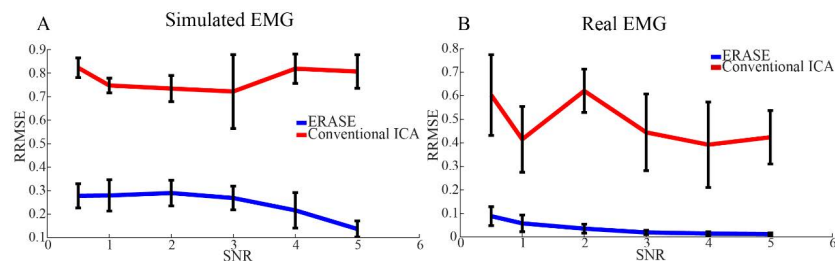


Figure 12. Relative root mean squared error (RRMSE) with varying SNR. A. RRMSE after running ERASE (blue line) and conventional ICA (red line) in the simulated EMG condition (simulated EMG was considered as contaminant). B. RRMSE after running ERASE (blue line) and conventional ICA (red line) in the real EMG condition (real EMG was considered as contaminant). The definition of RRMSE and SNR here can refer to literatures [1,38]. 200 simulated EEG were generated by the method described in Method in manuscript. Each EEG was contaminated by simulated EMG and real EMG, respectively, with different SNRs (0.5, 1, 2, 3, 4, 5). Each contaminated EEG was subjected to ERASE and conventional ICA, respectively, and artifacts-free EEG data

can be obtained. RRMSE was calculated for each artifacts-free EEG. Mean and standard deviation of RRMSE were calculated across those data with same SNR.

Table 1. Average false positive threshold for two variables

Number of contaminated EEG electrodes					
Parameter value	6	12	18	24	30
Average threshold	0.2886 ± 0.0034	0.2886 ± 0.0035	0.278 ± 0.0031	0.2885 ± 0.0033	0.2886 ± 0.0035
Number of added EMG channels					
Parameter value	1	2	3	4	5
Average threshold	0.2887 ± 0	0.2886 ± 0.0031	0.2885 ± 0.0033	0.2886 ± 0.0032 &	0.2887 ± 0.0035

mean ± S.D.

The threshold was defined as 5% of the maximal noise coefficient in the noise ICs column.

For the test of contaminated EEG electrodes, three types of EMG (simulated EMG signals from frontalis, temporalis, and posterior head muscles) were used.

For the test of added EMG channels, each type of EMG was employed to contaminate 6 EEG electrodes.

Table 2. Average sensitivity threshold for two variables

Number of contaminated EEG electrodes					
Parameter value	6	12	18	24	30
Average threshold	0.3664 ± 0.0031	0.3665 ± 0.0031	0.3664 ± 0.0032	0.3663 ± 0.003	0.3663 ± 0.0028

Number of added EMG channels					
Parameter value	1	2	3	4	5
Average threshold	0.242 ± 0	0.2864 ± 0.0001	0.3274 ± 0.0005	0.3896 ± 0.00032	0.4583 ± 0.00052

mean ± S.D.

The threshold was defined as 5% of the maximal noise coefficient in the noise ICs column.

For the test of contaminated EEG electrodes, three types of EMG (simulated EMG signals from frontalis, temporalis, and posterior head muscles) were used.

For the test of added EMG channels, each type of EMG was employed to contaminate 6 EEG electrodes.

Table 3. Average noise index for two scenarios

Number of contaminated EEG electrodes					
Parameter value	6	12	18	24	30
Average noise index (After ERASE with simulated EMG)	92.0419 ± 12.084	54.9098 ± 7.6664	40.2554 ± 6.0737	31.3284 ± 4.8454	25.3174 ± 3.8913
Average noise index (conventional ICA)	10.5437 ± 7.9094	5.8600 ± 3.7891	3.8574 ± 2.4690	3.1893 ± 1.8570	2.4541 ± 1.1627

Number of added EMG channels

Parameter value	1	2	3	4	5
Average noise index (After ERASE with simulated EMG)	33.4363 ± 6.9448	39.8032 ± 6.2961	37.7042 ± 7.9054	32.5832 ± 5.2438	39.7336 ± 9.6851
Average noise index (conventional ICA)	26.0746 ± 11.839	28.4582 ± 12.895	24.8897 ± 12.24	25.4884 ± 8.9587	27.7924 ± 8.8771

mean ± S.D.